Welding in the World (2023) 67:109–139
https://doi.org/10.1007/s40194-022-01369-3

RESEARCH PAPER

Distortion simulation of gas metal arc welding (GMAW) processes for automotive body assembly

Wayne Cai[1] · Miguel Saez[1] · Patrick Spicer[1] · Debejyo Chakraborty[1] · Richard Skurkis[1] · Blair Carlson[1] · Fernando Okigami[2] · Jeff Robertson[2]

Received: 4 February 2022 / Accepted: 18 August 2022 / Published online: 15 November 2022

Abstract

Welding-induced distortion is a major concern in the assembly of automotive components. Finite element-based welding simulation plays an important role in predicting the distortion so that the welding process can be modified during the design phase to alleviate the distortion experienced in production. In this work, gas metal arc welding (GMAW)-induced distortion was modeled and simulated for two HSLA steel welding cases as commonly seen in automotive body assembly. First, a "straight-clamshell" GMAW process was simulated and then validated against the measured temperatures, displacements, clamping forces due to thermal stresses at clamping positions, and weld penetration under various welding conditions. The numerical model captured the different strategies of welding directly versus tacking the parts first, resulting in 8 mm versus less than 2.0 mm of maximum distortion respectively. By overlaying resulting shapes from both simulation and laser scan measurement, it was confirmed that simulation can predict welding-induced distortion with sufficient accuracy. The simulation capability was further evaluated through a complete production case of truck rails welding. The same methodology was applied to compare simulation results (shape) with laser scan measurement data. Both simulation and test results confirm that welding distortion is greatly affected by boundary conditions, welding parameters, and welding sequence, all of which support simulation of the dimensional impact of welding in the manufacturing process design stage.

Keywords GMAW · Welding simulation · Distortion · Finite element analysis

1 Introduction

Gas metal arc welding (GMAW) is a welding process in which an electric arc forms between a wire electrode (filler) and the workpiece metals. This arc heats the workpiece metals to their melting point, causing them to fuse and create a joint. In GMAW welding, the thermo-mechanical behavior of materials is the most important factor in determining the weld quality. It should be carefully considered to avoid thermal distortion and residual stresses that impact dimensional and structural integrity. Moreover, because the GMAW process always melts the materials, it involves phase transformation where the microstructure changes, and thus, the mechanical properties of the materials may significantly differ from those at room temperature. Thermal distortions during welding highly depend on boundary conditions of the workpiece, welding sequence, and welding parameters such as heat input and welding speed. Understanding the thermo-mechanical behavior of materials and predicting distortion under different welding conditions are important to improve the manufacturing process.

The design of a welding process relies heavily on operator experience and a time-consuming trial and error approach which are inefficient and costly. As a solution to this, finite element analysis (FEA) based welding simulation has become a viable option for understanding the thermo-mechanical behavior of welded parts and predicting thermal distortion that may occur during welding. In addition, through welding simulations under various welding conditions, optimal welding process designs can be determined

Recommended for publication by Commission XII - Arc Welding Processes and Production Systems.

✉ Wayne Cai
wayne.cai@gm.com

1 General Motors Global R&D Center, Warren, MI, USA

2 MSC Software and Hexagon AB, Surrey, UK

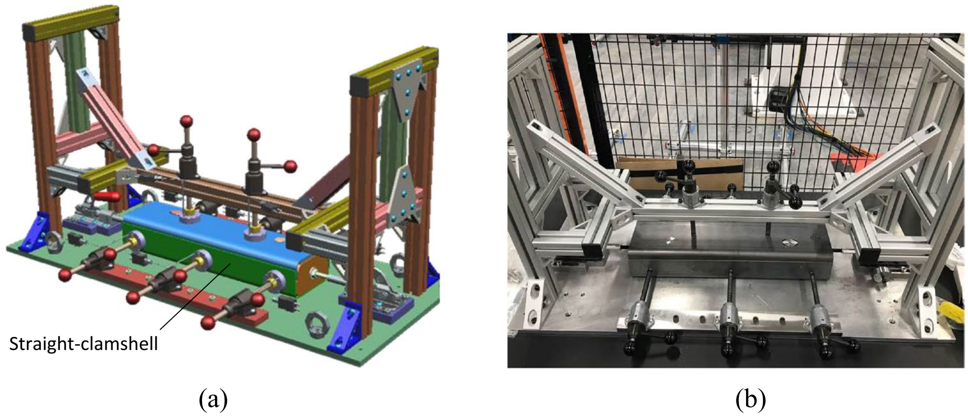

Fig. 1 Straight-clamshell assembly: CAD model (a) and actual built (b)

Table 1 Mechanical properties and chemical composition of A1011 HSLA grade 50 [27]

Tensile strength				Min. 420 MPa [60 ksi]		
Yield strength				Min. 345 MPa [50 ksi]		
Elongation				Min. 22% in 2 in. [21 mm]		
Chemical composition						
C	Mn	P	S	Ni	Cr	Mo
0.15%	1.65%	0.02%	0.025%	0.2%	0.15%	0.16%

prior to actual manufacturing. However, welding simulation is a difficult problem as the thermo-mechanical behavior of weld parts is a multi-physics problem by nature and highly nonlinear as well involving phase transformation and plastic deformations of the weld parts. Since the early work by Ueda and Yamakawa [1] and Hibbit and Marcal [2] on numerical simulation of welding by FEA, a great amount of work has been reported. Lindgren [3–5], in his three parts papers, reviewed a large number of articles on finite element modeling and simulation of welding, published in years up to 2000. The author also presented a comprehensive list of modeling and analysis issues related to FEA-based simulation of welding.

In order to predict welding-induced plastic strains and residual stresses for thin metal welding, Michaleris et al. [6, 7] developed a two-step decoupled approach using thermo-mechanical FEA. Tsai et al. [8] studied the distortion mechanism and the effect of welding sequence on thin panel distortion using a finite element model. Welding-induced buckling distortions and mitigation techniques were discussed by Yang and Dong [9] based on finite element welding simulations of thin-section structures. FEA-based welding simulations of large-scale structures are quite costly in terms of computational resources and time. In an effort to reduce computation time, Huang et al. [10] developed a dynamic mesh refining method (DMRM) and proposed a dual-mesh

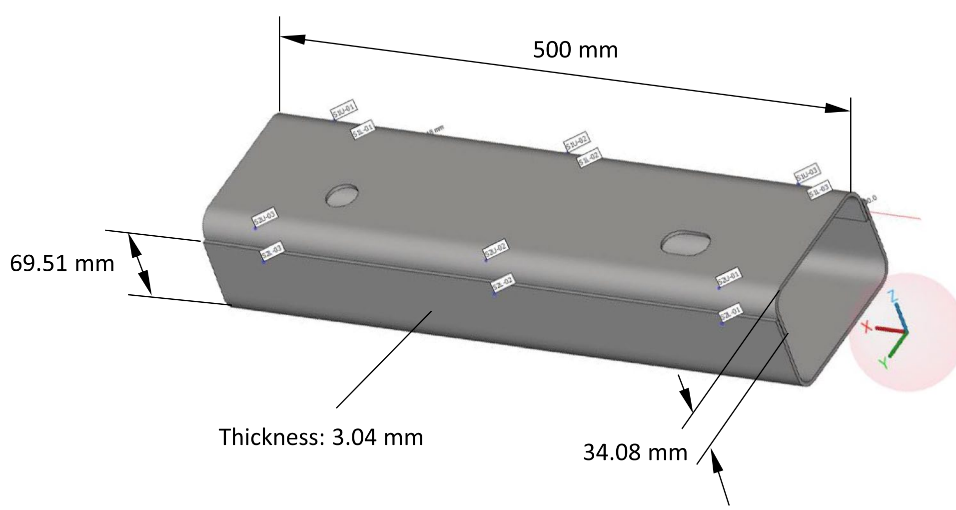

Fig. 2 Straight-clamshell model

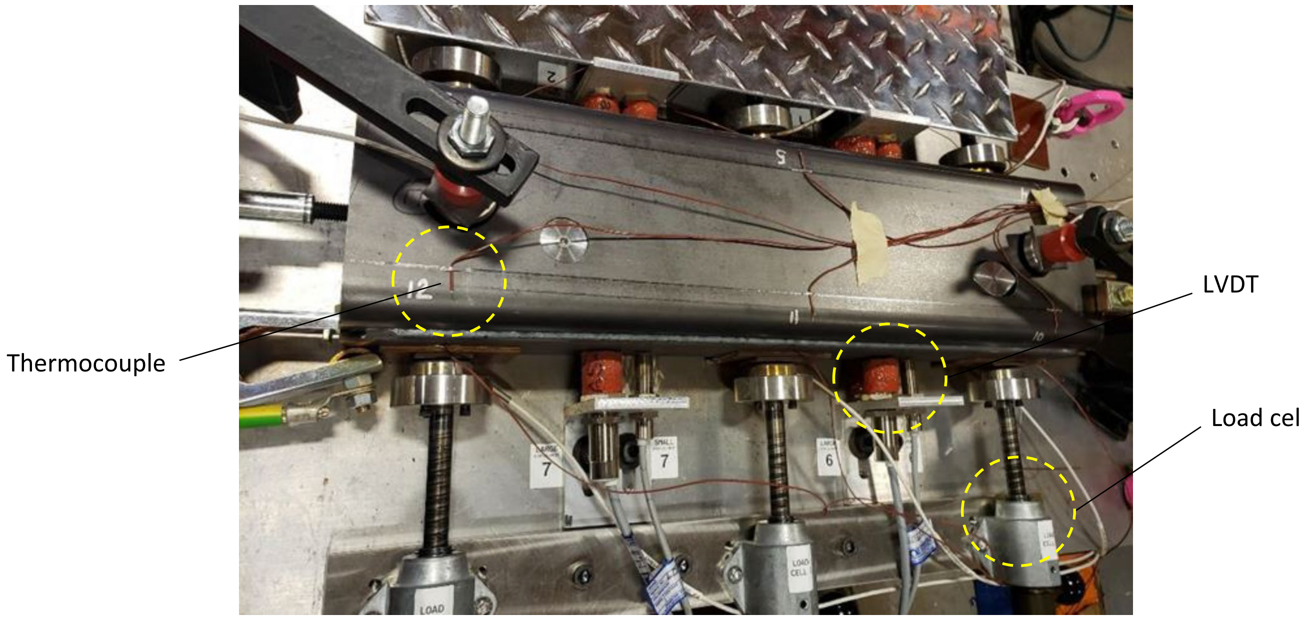

Fig. 3 Instrumentation: load cells, LVDTs, and thermocouples

heat transfer method which accelerated the computation time by 10 times over the conventional FEA model [11]. For thin-walled structures, high prediction accuracy can be obtained by using shell-element-based models within even less computational time [12–14].

Welding distortions and residual stresses can be minimized by the welding process and parameter control. For example, the rate of heat input and welding speed affect distortion [15, 16]. Chen et al. [17] demonstrated that welding sequences in addition to welding speed and heat input influenced welding deformations and residual stresses. In welding processes, clamping is often required to control welding distortions; however, it induces residual stresses in general. Schenk et al. [18, 19] reported experimental and numerical studies on the influence of clamping on welding distortion, where a 1-mm DP600 overlap joint and a 6-mm S355 T-joint were used to study the effects of clamping time, release time, and the influence of clamp preheating. A numerical and experimental study addressing the effect of jig position and pitch on welding-induced deformation during plate welding was presented by Ma et al. [20]. Through numerical simulation and experimental validation, Zhang et al. [21] investigated the effectiveness of the structural restraint method and the presetting method for reducing welding angular distortion and residual stresses in thick-plate T-joint welding, where the study concluded that the presetting method is more effective in reducing the angular distortion than the structural restraint method while neither method is effective in mitigating residual stresses. It should be noted that the outcomes of these works were mostly based on simple and symmetric structures. Therefore, the existing experience in reducing welding-induced distortion

Fig. 4 Data acquisition (DAQ) system diagram

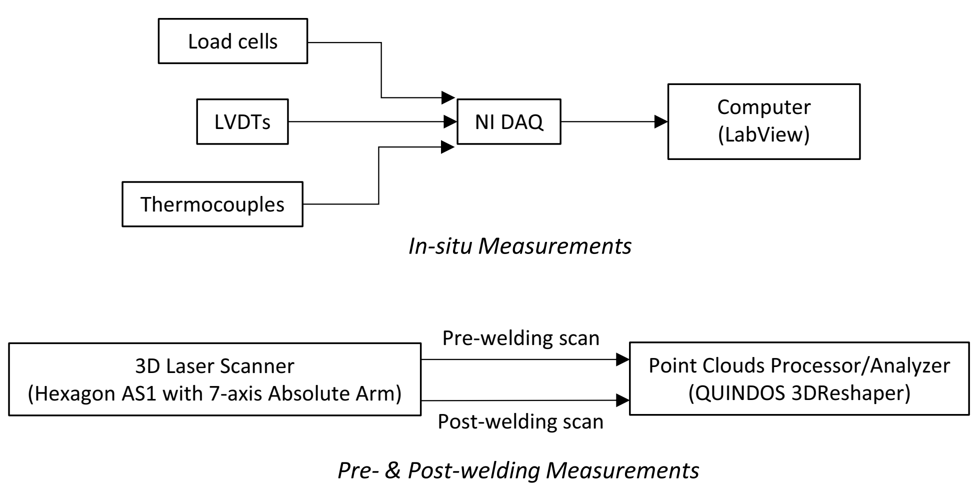

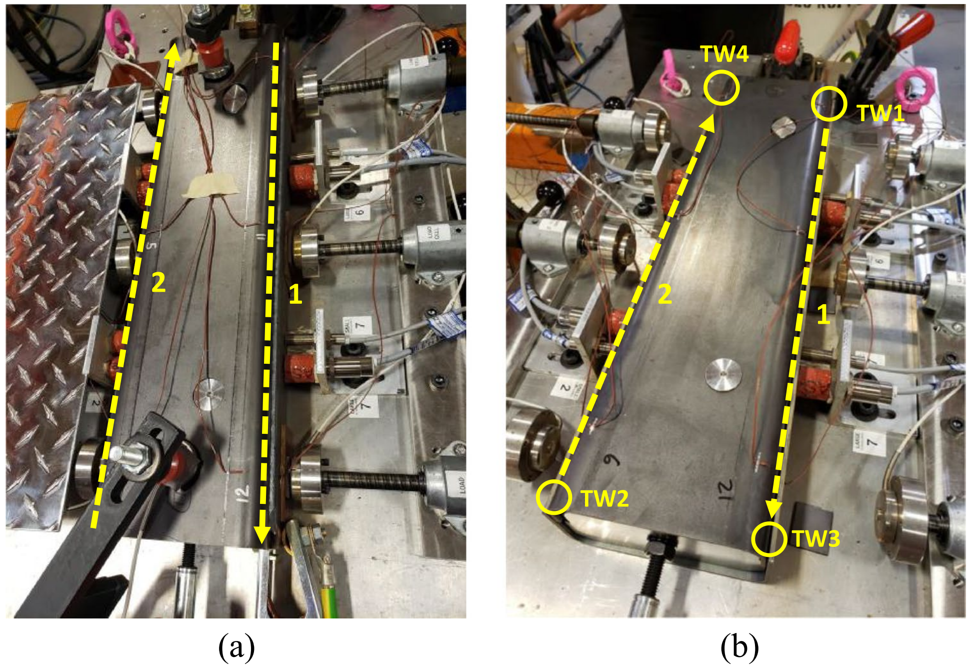

Fig. 5 Test setup for (a) Case 1 and (b) Case 2

requires further validation through extensive simulations and experiments before application to complex automotive component manufacturing [22].

Commercial FEA software can be used to simulate welding-induced distortion, including general purpose solvers such as *ABAQUS*, *ANSYS*, and *LS-Dyna*, and welding specialty solvers such as *Simufact Welding* and *SYSWELD*. To enhance modeling efficiency and avoid modeling errors, welding specialty solvers have become preferred choices in industries where lead-time is critical and a thorough understanding of the multi-physics nature of welding is not required. Thater et al. [23] simulated the distortion of a car door induced during remote laser welding with various welding sequences, weld length, and positions and reported the effect of heat input control on the distortion. Perret et al. [24] predicted the distortion of an automotive cross member where inserts were welded by GMAW and showed that consideration of experimental heat distribution for calibration of the heat source has a significant effect on the accuracy of prediction. Nateghi and Volukola [25] investigated the effect of weld configuration geometry on the residual stress distribution and temperature history during gas tungsten arc welding. Optimization of welding process parameters was conducted by Islam et al. [26] by integrating *Simufact Welding* with MATLAB where voltage, current, velocity, and a limited case of welding direction were considered as design variables.

The finite element method for welding simulations has significant merit for designing an optimal and cost-effective welding process, provided, however, that its capability and limitations under various welding conditions are fully understood. In this paper, the modeling capability of this commercial software package for the prediction of distortion induced during GMAW is evaluated under various welding conditions and its simulation results are compared with actual welding test data, using a carefully designed test setup and workpiece named “straight-clamshell” which

Table 2 Welding parameters for cases 1 and 2

Voltage (V)	22.0
Current (A)	185.0
Speed (mm/s)	10.0
Filler wire diameter (mm)	1.2

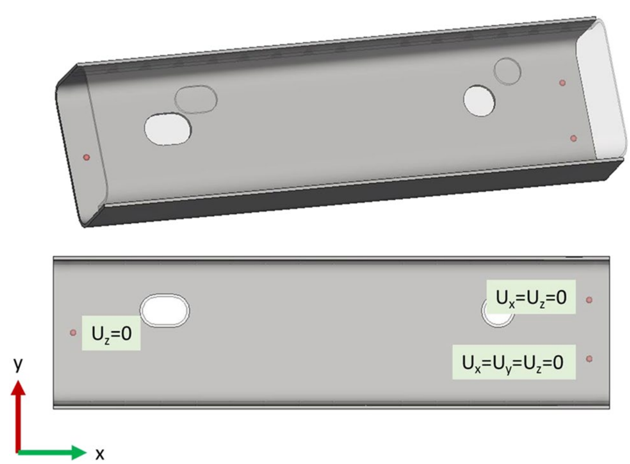

Fig. 6 Locating scheme

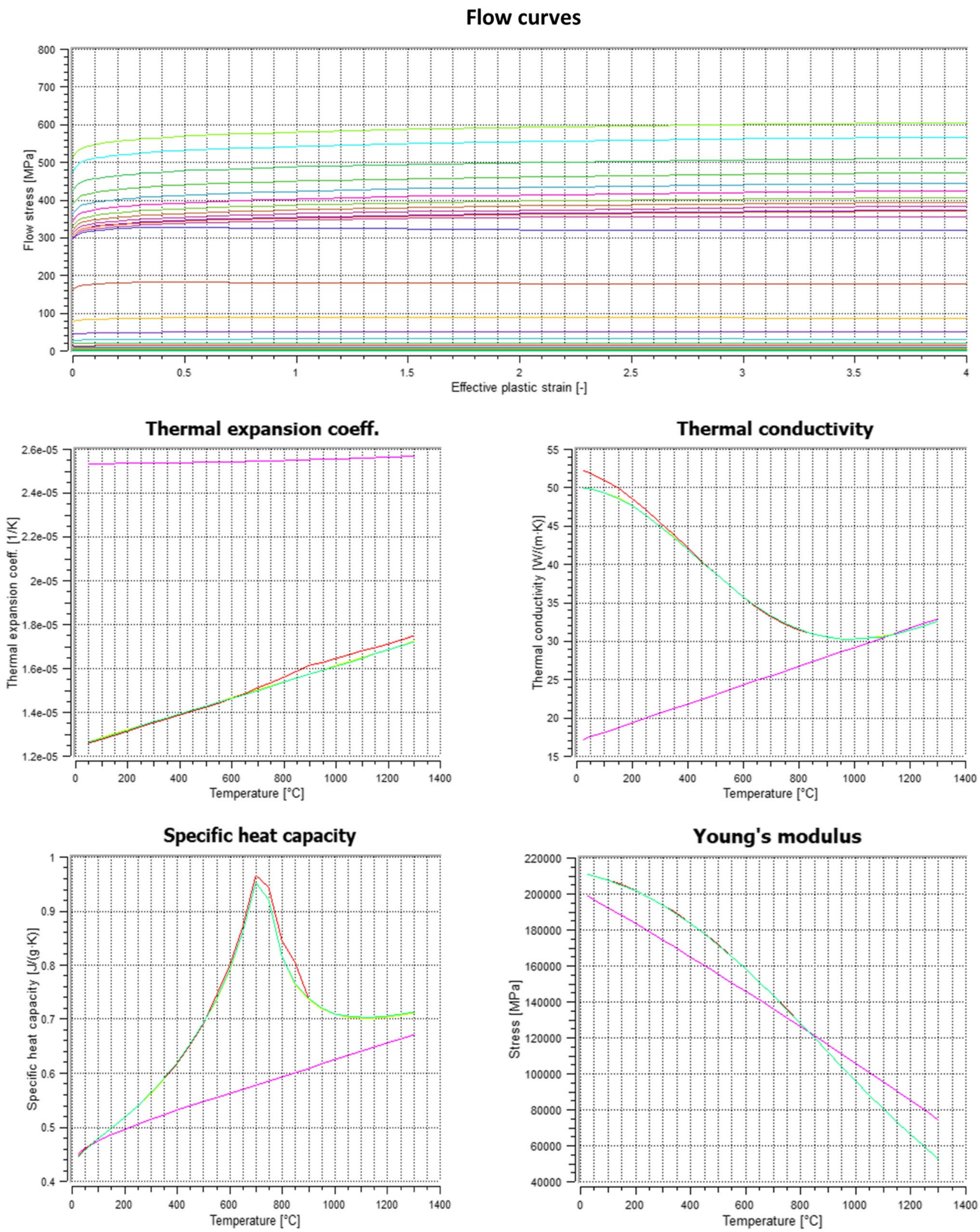

Fig. 7 Thermomechanical data calculated by JMatPro® and curated using available mechanical test data

Table 4 Heat source definition

Voltage (V)	22.0
Current (A)	185.0
Speed (mm/s)	10.0
Efficiency	0.95
Front length	2.0
Rear length	6.0
Width	3.3
Depth	4.4
Gaussian parameter	0.0

represent the geometrical characteristics and welding process of truck frame rails. The software's modeling and simulation capability for the prediction of distortion are further examined through the welding simulation of the production-level truck frame rails. The goal of this work is to demonstrate that a well-established commercial FEA package tailored for manufacturing simulation can be used to predict distortion confidently and therefore there is no need to keep validating its efficacy.

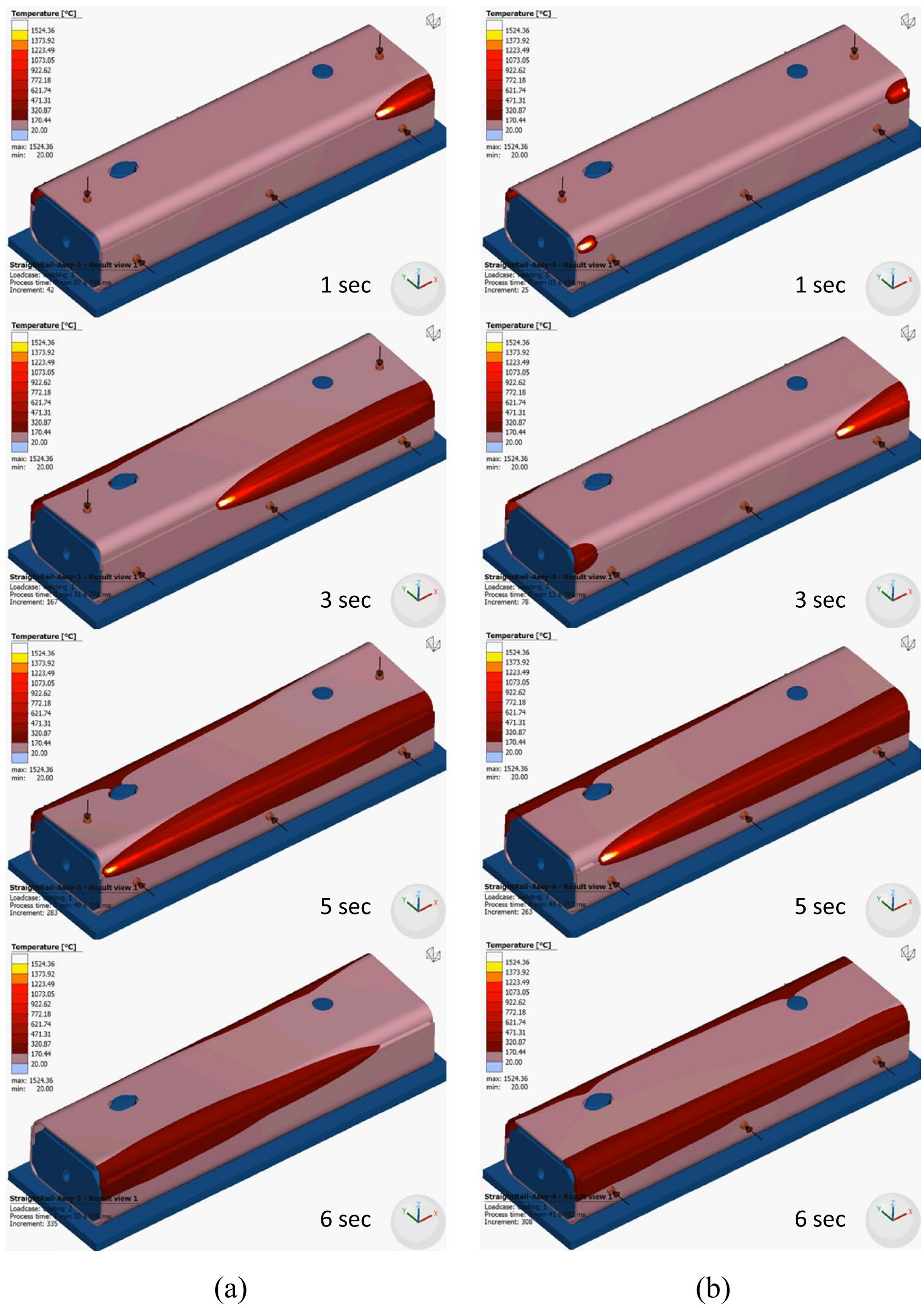

Fig. 8 Temperature distribution simulation for a case 1 and b case 2

2 Straight-clamshell simulation and validation

This section describes the modeling and simulation of the "Straight-Clamshell" GMAW distortion using the finite element method (FEM) followed by a comparison of simulation results with actual welding test data in terms of temperature distribution, thermal distortion, clamping force, and weld penetration. The part configuration in this setup is representative of automotive truck frame rails.

2.1 Welding test setup

A welding test setup with a state-of-the-art data acquisition system was designed and built for the validation of numerical simulation results as described below.

As can be observed in Fig. 1, the straight-clamshell assembly consists of two U-section channels which are joined by two welding robots. The upper and lower U-channels are made of the same steel sheet of 3.04 mm thick, A1011 high-strength low-alloy (HSLA) steel of grade 50. The mechanical properties and chemical composition of the material are listed in Table 1 and the overall dimensions are presented in Fig. 2. The welding fixture supports the assembly at up to 8 positions with clamps during welding as can be observed in Fig. 1.

Referring to Fig. 3, attached to each clamp is a load cell that measures the force normal to the channel surface and which is generated by welding distortion. As can be observed in the figure are 4 displacement sensor (linear variable differential transformer, LVDT) arrays that are placed with the purpose to measure the normal displacements created by distortion during welding of the lower channel; however, it was found that these LVDTs became faulty due to overheating during the weld tests and their measurements were erroneous. Therefore, instead, the distortion of the assembly is measured using a Hexagon 3D imaging laser scanner to compare with the results from numerical simulation. In addition, the temperature distribution in the assembly during welding was measured at 12 different points by using the thermocouples affixed to the channel surfaces, refer to Fig. 3. A diagram of the data acquisition system with brief descriptions of the probing devices and signal processing equipment is presented in Fig. 4. Note that the data were subsequently filtered and down sampled by a factor of 25 twice using an 8th-order Butterworth filter with a cut-off frequency at 1/50 of the sampling frequency. The load cell data were smoothed using 4-tap and 16-tap moving average filters, respectively. The temperature data did not require filtering. To ensure capturing of any significant transient behavior without loss or

Table 3 Heat transfer coefficients

Convective heat transfer coeff. h	Contact heat transfer coeff. α	Emission coeff. ε
20 W/m^2 K	1,000 W/m^2 K	0.3

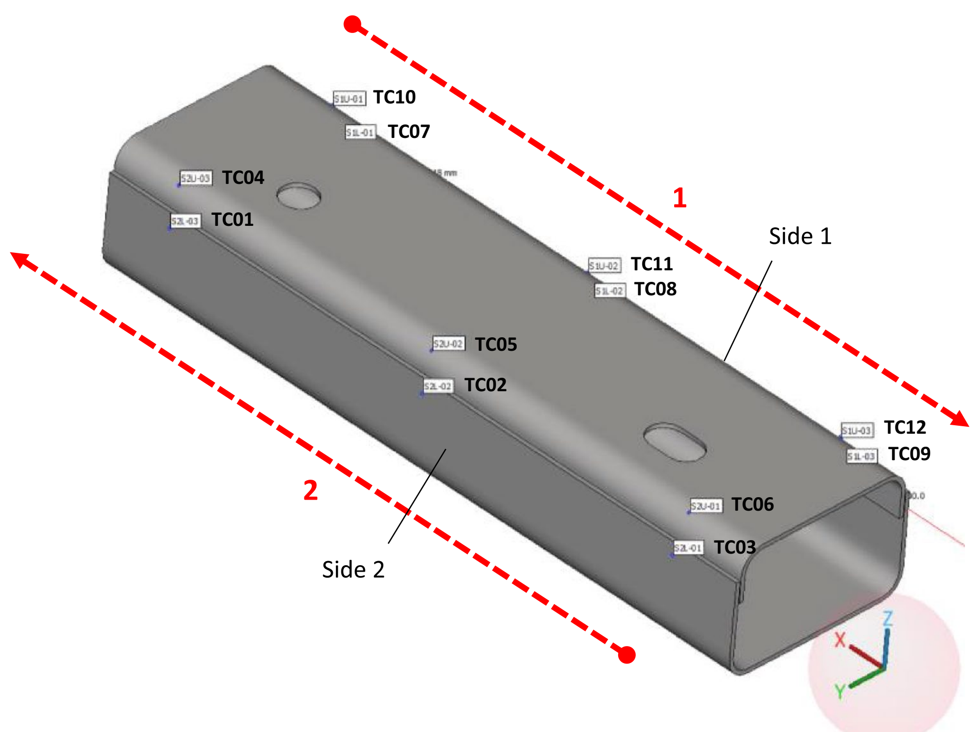

Fig. 9 Locations of 12 thermocouples

distortion, each filter was applied twice in a phase-compensating manner to obtain a phase invariant response.

A total of 8 validation tests were performed under different welding conditions. Two representative cases, which are referred to as case 1 and case 2, are presented in this paper. For case 1, refer to Fig. 5a, the channels were fully clamped at 8 points without tack welds. The dashed arrow lines indicate the welding sequence with 1 s time delay between the two weld paths. For case 2, refer to Fig. 5b, the top 2 clamps were removed after tack welding (12–17 mm in length) the 4 corners of the lower channel. The two corners marked as TW1 and TW2 in the figure were first tack welded simultaneously, and then, TW4 was added after TW3 with about a 1-s delay. The welding parameters were calibrated using General Motors standards for 4-mm sheet thickness and used for both cases 1 and 2 and are listed in Table 2.

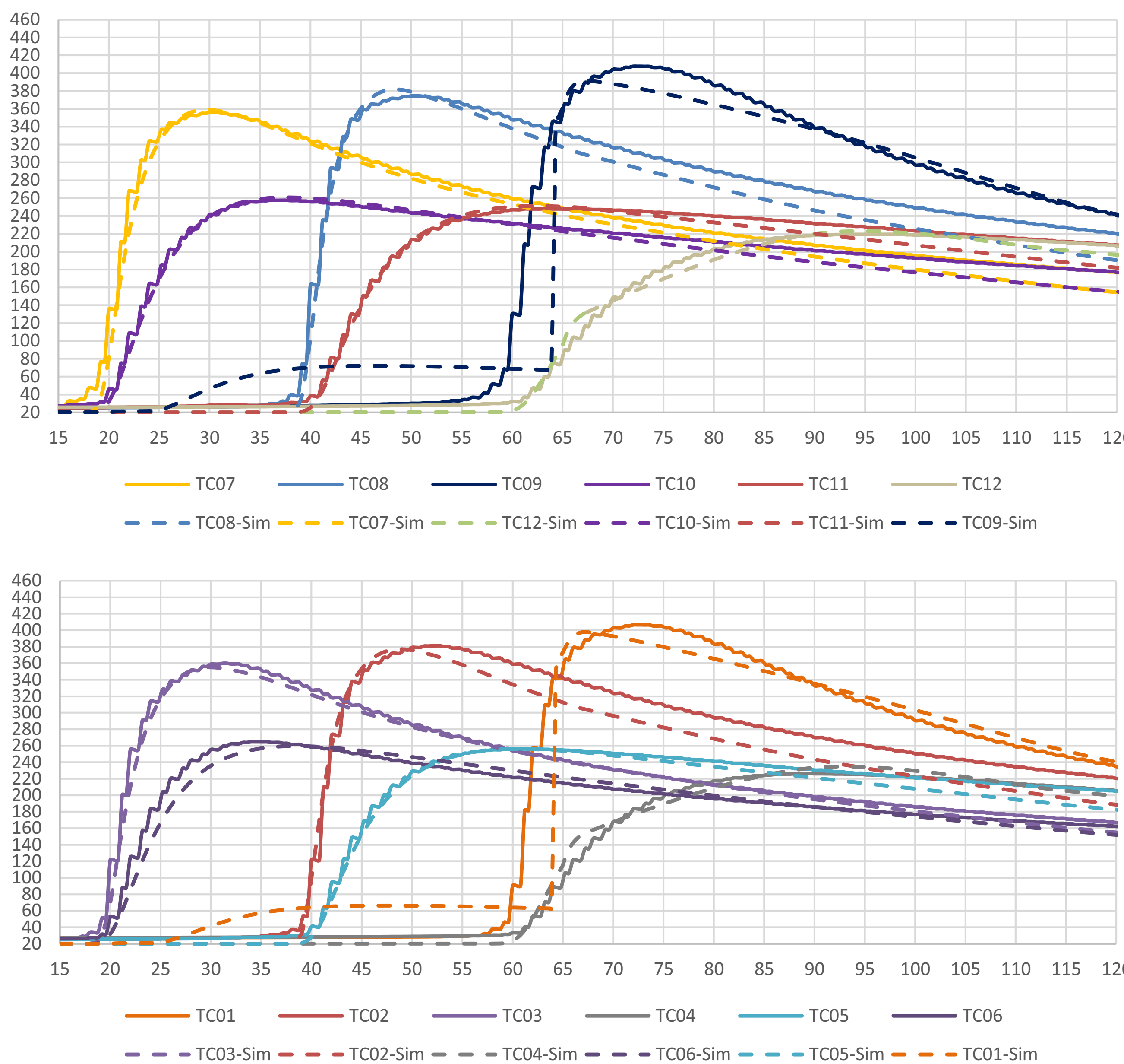

Fig. 10 Comparison of temperature histories (°C vs. seconds) between test (solid curves) and simulation (dashed curves) for case 1

2.2 Numerical simulation model

2.2.1 Mesh and element selection

The FEA software utilizes a subset of element types available in the general-purpose MSC Marc solver [28]. These elements are focused on 3-dimensional continuum mechanics supporting both thermal and structural aspects of modeling. All heat transfer element types available have a complementary stress element type ensuring compatibility in data exchange during a coupled thermomechanical analysis.

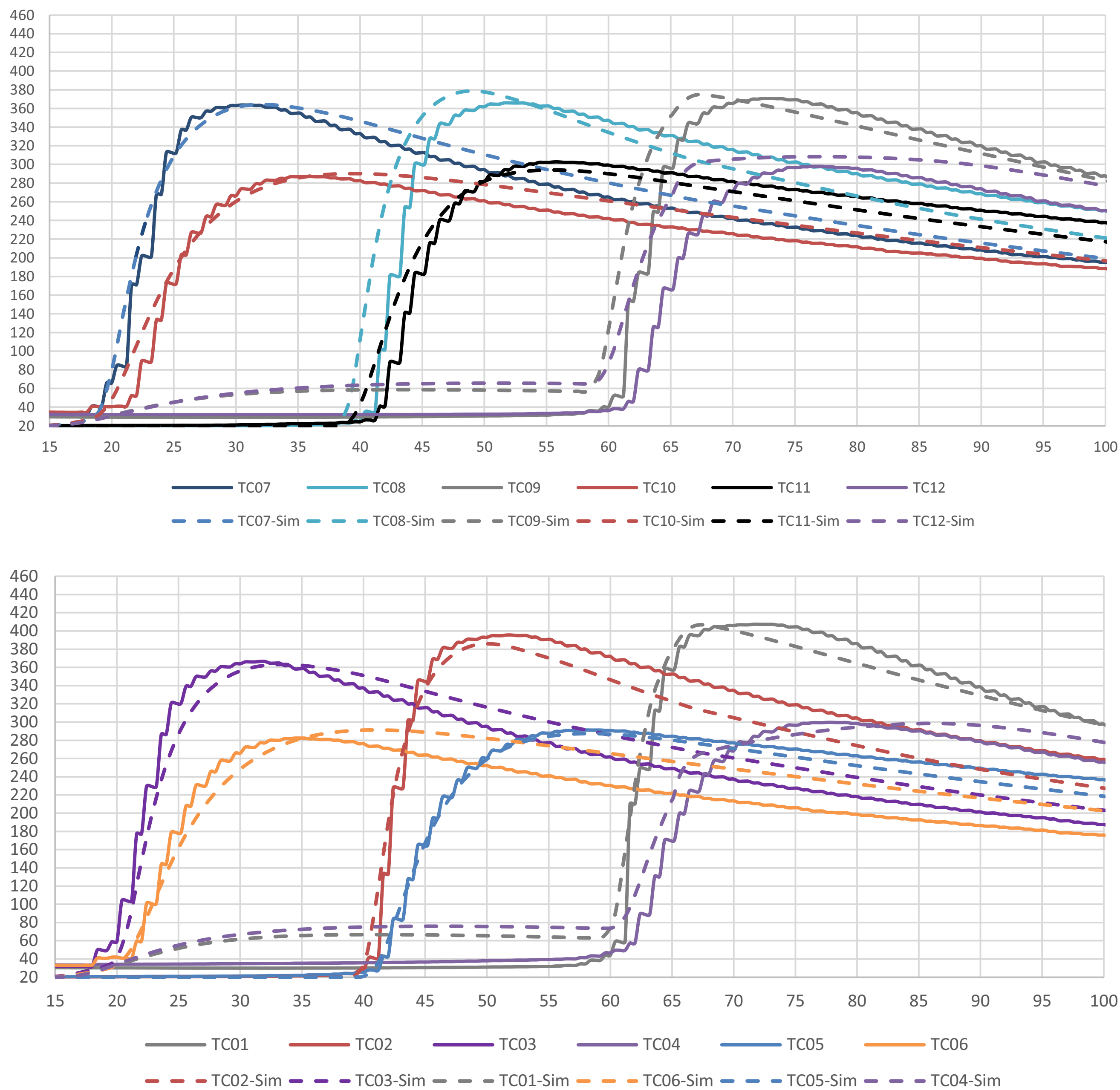

Fig. 11 Comparison of temperature (ºC vs. seconds) histories between test (solid curves) and simulation (dashed curves) for Case 2

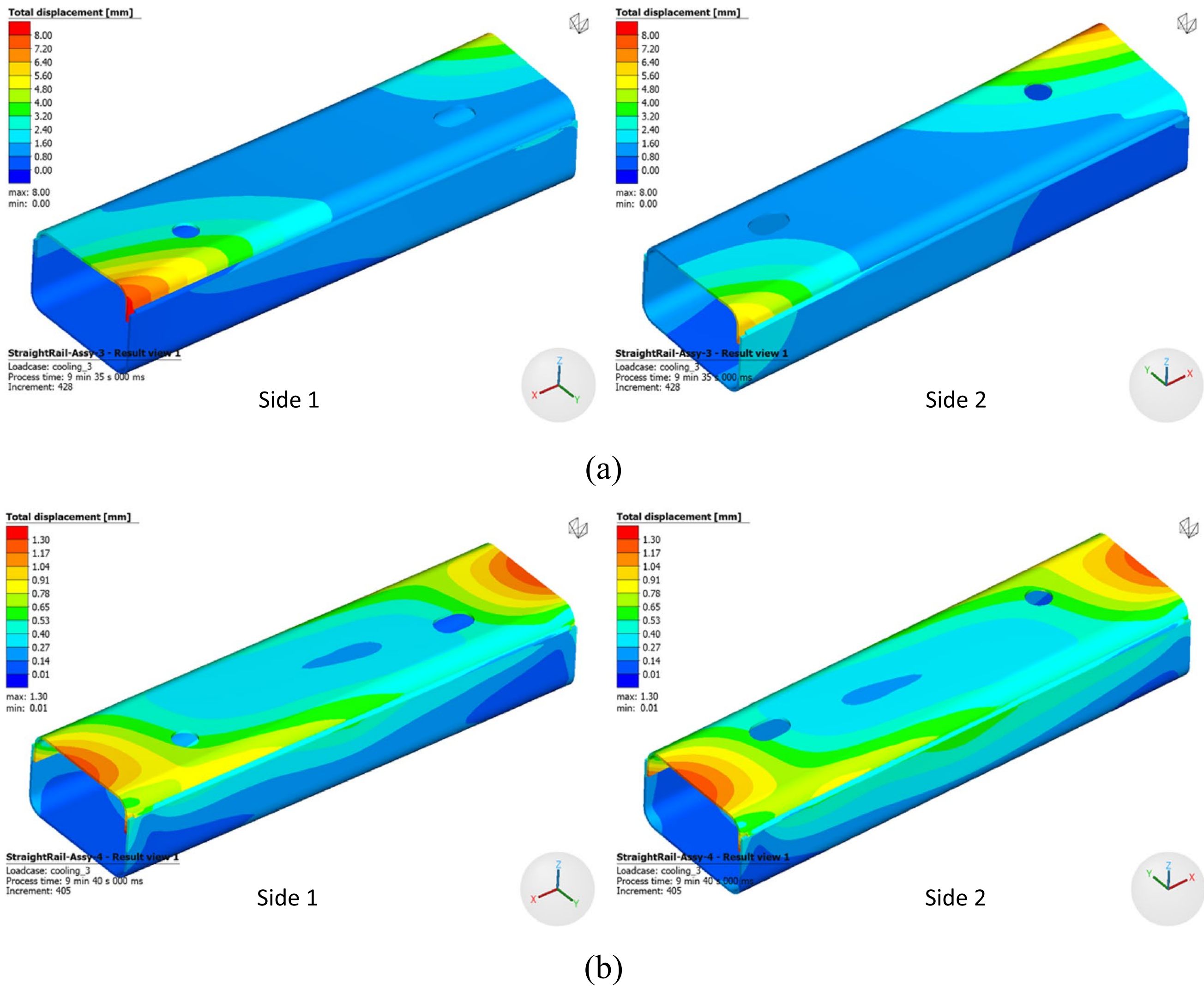

Fig. 12 Displacement field for (a) Case 1 and (b) Case 2

In large deformation analysis, linear elements with linear shape functions are preferred due to their numerical robustness with respect to mesh (physical) distortion. For this reason, no high-order element types were used in this work. To model both components and weld beads, a pure hexahedral mesh was created using element #7 (thermal) and element #43 (structural). Prior to the analysis, the entire model needs to be meshed, which also includes the weld filler. For the filler metal, however, it is not required nor desired for its elements to be active throughout the entire simulation. They should not be subjected to boundary conditions or participate in heat transfer or structural analysis before their physical creation by the weld power source. The quiet element method implemented in the numerical solver captures this

Fig. 13 Maximum distortion for (a) Case 1 and (b) Case 2

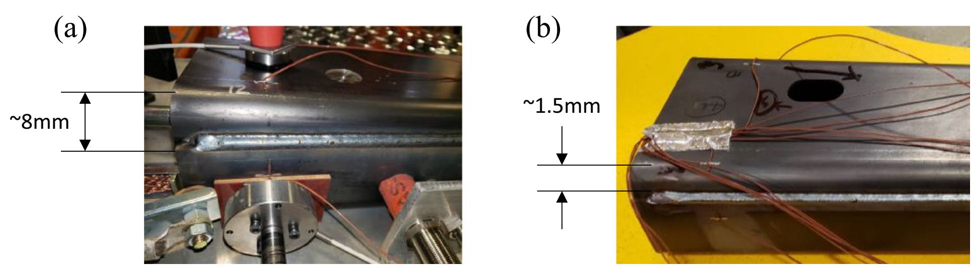

expected behavior as the weld filler elements only become active at or above the melting point. Until that point, the contacting region is treated as an exposed surface. To ensure that contact conditions and proper temperatures are met, filler elements will always participate in the analysis, hence they do not behave as deactivated elements. Their physical properties, however, are reduced until they become thermally activated by the heat source. If an element is in a quiet state, its thermal expansion coefficient is set to zero and all other material properties (except for yield stress, specific heat and density) are scaled down by a factor of 1E−5. This scaling is applied to the reference values at room temperature and all other temperature dependencies are ignored. For the activation to happen, the heat source is associated with a filler bounding box in a local cartesian coordinate system attached to the heat source. Thermomechanical properties of filler elements falling within this bounding box are then restored by the solver during calculation.

2.2.2 *Thermal solution* [28]

Temperature represents the central quantity for thermal calculations. With given nodal temperatures T, the temperature distribution $T(x)$ inside an element is interpolated via the shape functions $N(x)$ as:

$$T(x) = N(x)T$$

As heat capacity $C(T)$ and thermal conductivity $K(T)$ are both temperature-dependent, the governing equation for heat transfer is then:

$$C(T)\frac{dT}{dt} + K(T)T = Q$$

Q is the heat flux vector or tensor depending on dimension.

The backward difference scheme is applied to divide the time into discrete time steps Δt. For each increment number n, nodal temperature results from the following expression:

$$\left[\frac{1}{\Delta t}C(T) + K(T)\right]T_n = Q_n + \frac{1}{\Delta t}C(T)T_{n-1}$$

The solution to this expression requires evaluation of the temperature-dependent matrices C(T) and K(T). At the beginning of a new increment, an appropriate estimate is provided by linear extrapolation from the temperatures obtained on two preceding time steps. For each time interval τ within the current time increment, the required temperature follows:

$$T(\tau) = T(t - \Delta t) + \frac{\tau}{\Delta t}[T(t - \Delta t) - T(t - 2\Delta t]$$

During subsequent iterations of a given increment, the temperature within that time interval is based on the corresponding temperature $T^*(t)$ from the preceding iteration:

$$T(\tau) = T(t - \Delta t) + \frac{\tau}{\Delta t}\left[T^*(t) - T(t - \Delta t)\right]$$

With the above estimates for the nodal temperature, it is possible to obtain an average of the desired temperature-dependent material property f for the entire time interval via:

$$f = \frac{1}{t}\int_{t-\Delta t}^{t} f[T(\tau)]d\tau$$

2.2.3 Welding heat source

The Goldak's double ellipsoid [29] was used in this work to model a conventional arc welding heat source. When moving along the x direction, its shape is determined by the weld pool front length a_f, rear length a_r, width b, and depth d. These parameters are then combined to form two volumetric heat flux rates q_f and q_r for the weld pool heat distribution (see Table 4 for numerical values used to represent the heat source in this work).

2.2.4 *Thermal boundaries* [28]

All meshed components have free boundaries over which heat losses can occur via convection (free or forced) and radiation. Convective heat transfer depends on temperatures T and T_0 of the surface and its surroundings and it is governed by the following equation:

$$\frac{\dot{Q}_c}{A} = -h\left(T - T_0\right)$$

Emissivity is considered by including the Stefan-Boltzmann law as well:

$$\frac{\dot{Q}_r}{A} = -\varepsilon\sigma\left(T^4 - T_0^4\right)$$

where σ is the Stefan-Boltzmann coefficient, h is the convective heat transfer coefficient, ε is the material's emissivity coefficient, $\dot{Q}_c$ is the heat flux, and A is the applied area.

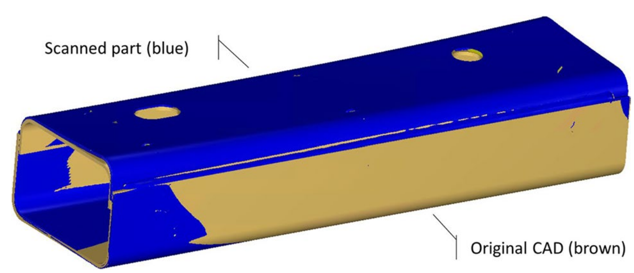

Fig. 14 Scanned point (blue) cloud aligned to the CAD model (brown) of case 1

Besides the equation above, Simufact has implemented its own proprietary formulation for contact heat transfer that considers the contacting pair’s thermal conductivity, temperature, contact pressure, and friction. This formulation is not openly available and could not be made public in this work. Suffice to say, the heat transfer (losses) coming from contact between deformable bodies and with boundary conditions is treated via this formulation.

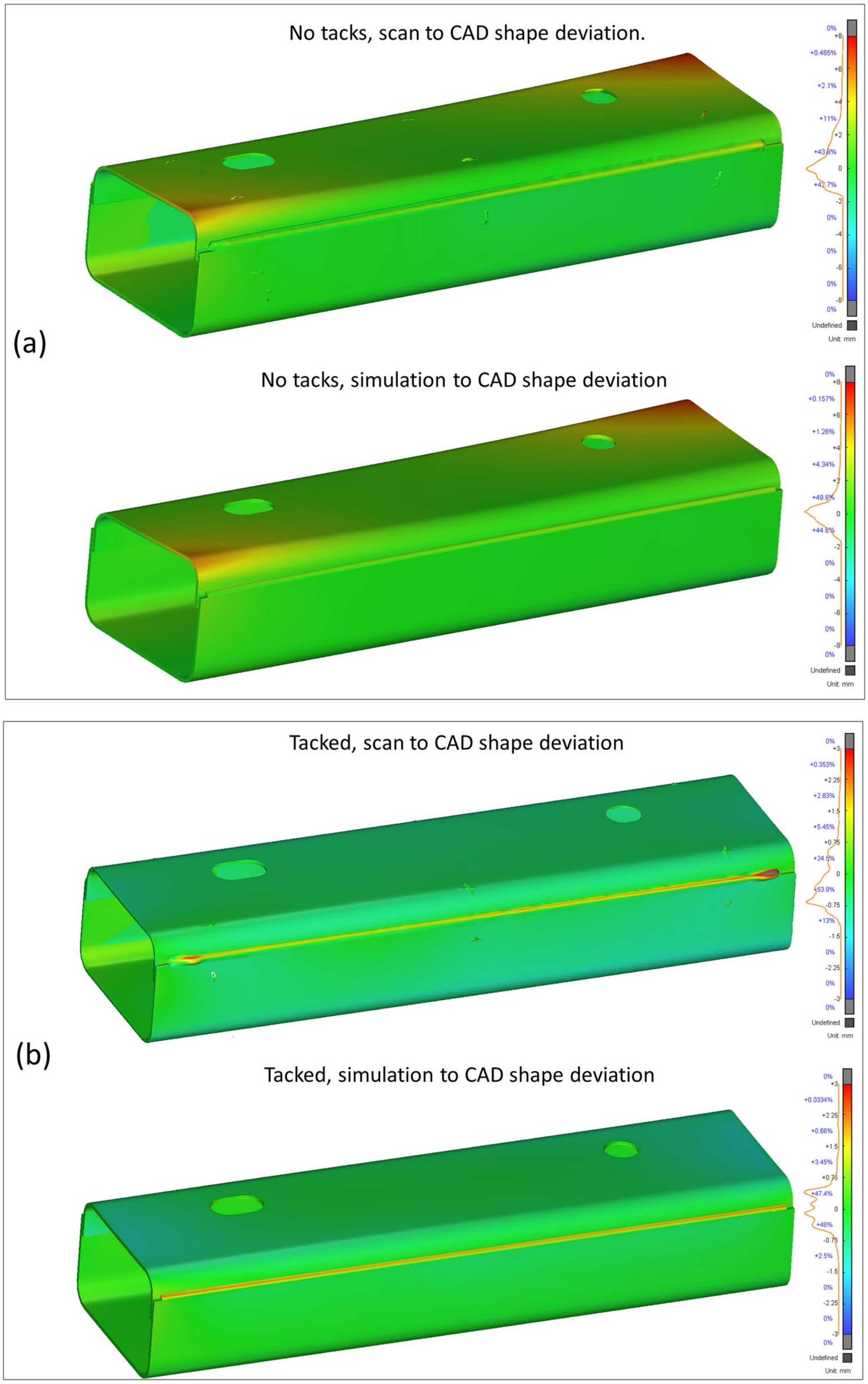

Fig. 15 Comparison of displacement field between simulation and scan data for case 1 (a) and case 2 (b)

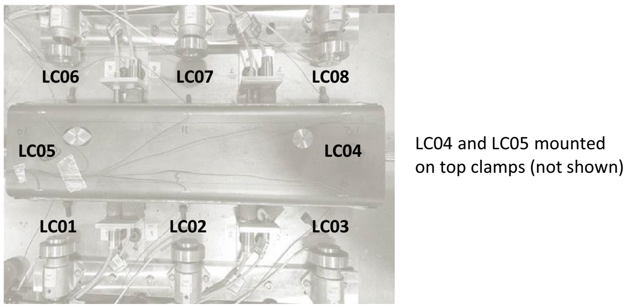

Fig. 16 Locations of 8 load cell

2.2.5 Numerical welding process model

The FEA model was created following the same physical setup to increase accuracy and enable direct correlation with experimental results. The two shells were meshed on MSC Apex which gives the user a good level of flexibility while keeping the modeling process simple. There is a toolkit specifically designed to mesh automotive components for welding analysis, this simplifies the process and saves time as meshing is a necessary step that usually requires some level of experience.

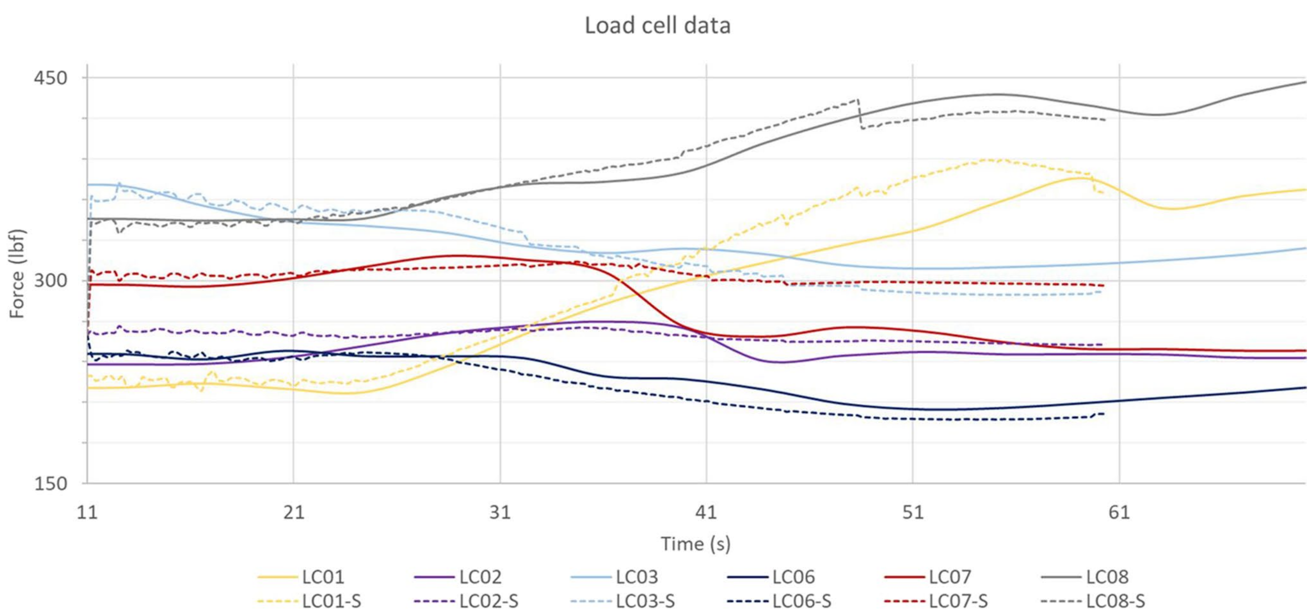

Fig. 17 Comparison of clamping forces between load cell measurements (solid curves) and simulation (dashed curves) for case 1

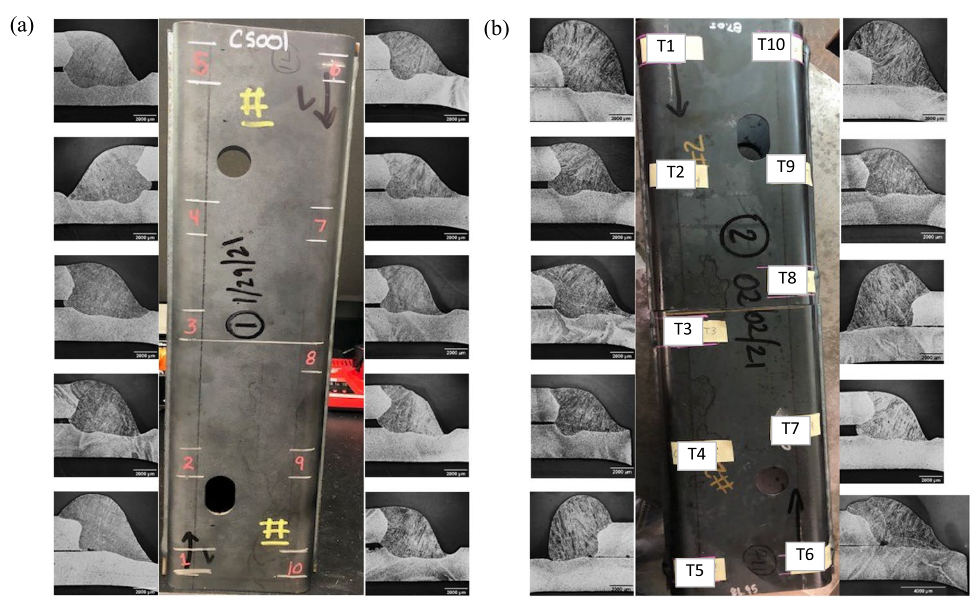

Fig. 18 Optical microscopic images of actual welds for case 1 (a) and case 2 (b)

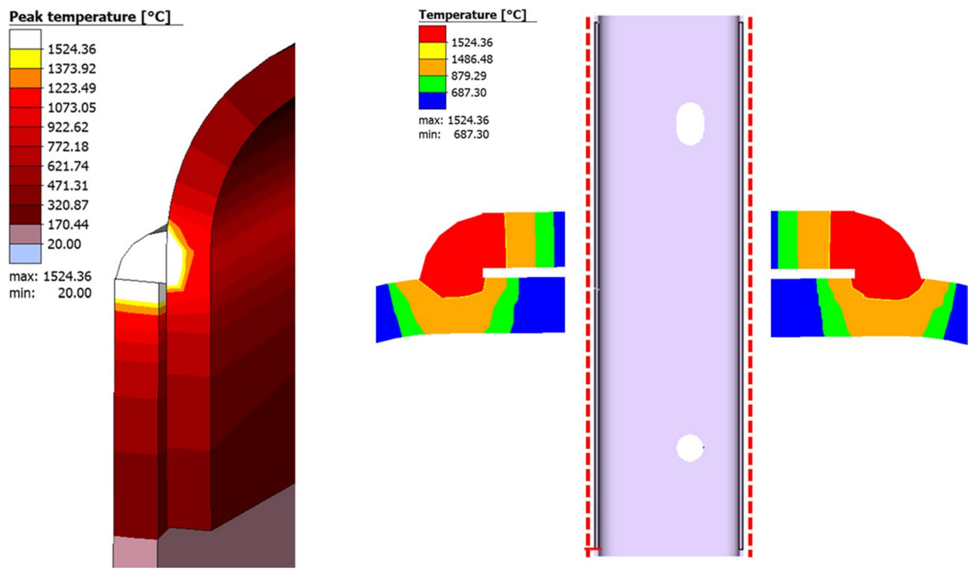

Fig. 19 Weld penetration simulation for case 1

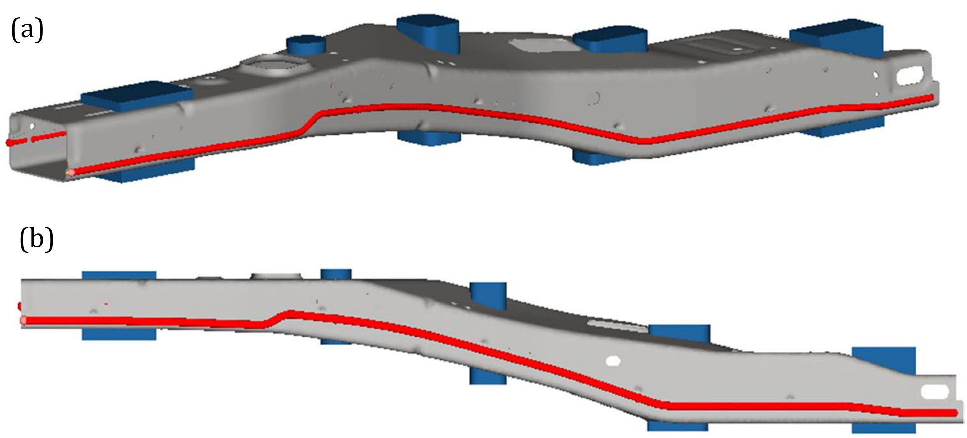

Fig. 20 Simulation model for truck rail: iso view (a) and x–y view (b)

For both U-channels and the filler, the element type selected is hexahedral (HEX8) that has eight nodes, full integration points, and double numerical precision definition. For heat-affected zones (HAZ), an element size of 1.5 mm was used. This element size then gradually grows to 4.5 mm to improve simulation efficiency. To accurately capture bending and twisting effects, both U-channels have two element layers through the thickness to avoid shear-locking effects. Based on an assembly sample, it was observed a 1 mm gap existed between the two U-channels. For modeling purposes, we considered 0.5 mm of gap on each side where the U-channels meet.

The analysis of contact behavior is complex because of the requirement to accurately track the motion of multiple geometric bodies and the motion due to the interaction of these bodies after contact occurs. Several methods have been developed to treat these problems including the use of perturbed or augmented Lagrangian methods, penalty methods, and direct constraints. The solver allows contact analysis to be performed automatically without the use of special contact elements. For this work, the segment-to-segment (S2S) contact algorithm is used as it provides a more robust way of detecting penetrating nodes and contact distance than the standard node-to-segment (N2S) algorithm. In the S2S algorithm, the nonpenetrating constraints are enforced using augmented Lagrangians; this implies that one can define deformable contact bodies

Table 5 Heat source parameters for the truck rail model

Voltage (V)	22.0
Current (A)	200.0
Speed (mm/s)	16.7
Efficiency	0.85
Front length (mm)	2.0
Rear length (mm)	8.0
Width (mm)	3.0
Depth (mm)	3.2
Gaussian parameter	0.0
Heat front scaling factor	0.4

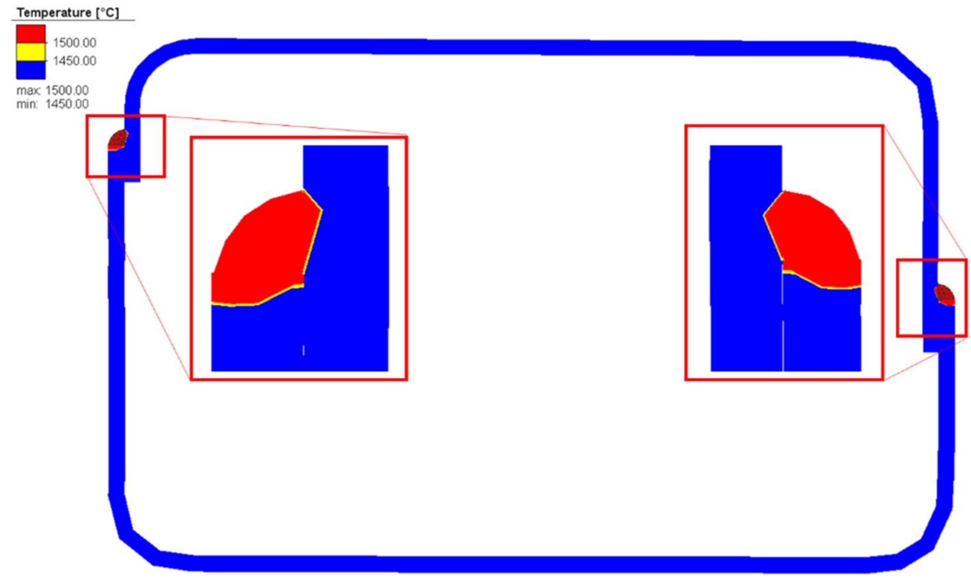

Fig. 21 Weld penetration for the truck rail simulation model

consisting of finite elements, and rigid bodies consisting of curves (2D) or surfaces (3D). Rigid bodies can be load, velocity, or displacement controlled. In this work, all rigid bodies, except for the clamps, do not apply any of these conditions. The initial contact table is established by a search algorithm and can be further modified by the user. As all models rely on contact calculation to reproduce realistic conditions, there is no need for a conformal mesh with nodal connectivity to be created. Relative movement between parts and boundary conditions is expected, by default the software utilizes the Coulomb friction model that is implemented as a bilinear function and the value of 0.3 is applied as the default global friction coefficient.

All geometrical boundary conditions such as clamps, bearings, and pins are treated as rigid bodies and are not required to have a volume mesh. In such cases, a surface mesh with an element size of 2.6 mm on average provided a closed surface definition for boundary conditions. This means such geometries provide only contact information for both thermal and mechanical solutions, there is no stress or temperature fields being solved for the geometries representing the boundary conditions themselves. In terms of model size, a total of 110,600 volume nodes and 71,246 volume elements were used for the U-channels and the weld beads. For the boundary conditions, 97,716 surface nodes and 99,081 surface elements were used.

Weld bead activation relies on temperature and creates a glue contact with adjacent bodies if they are within contact tolerance at the point in time where the temperature is greater than the melting point. This means, until the heat source reaches a certain location of the model, the elements of the weld beads remain in a quiet mode with extremely low mechanical properties. This is all automatically handled by the solver and there is no need for user intervention.

Bearings are rigid bodies with infinite stiffness and represent static objects in the model: 2-way, 4-way, and fixture base and table. Clamps have finite stiffness and can apply/react to forces in any direction. The two mandrels were modeled as clamps with lower in-plane stiffness and zero initial force as per prior structural study. The six side load cells (LC01-3, LC6-8) were modeled as clamps with 1E6 N/m stiffness and 200 lbf (890 N) of initial force. These forces were later updated based on load cell initial measured load. The two clamps on the top were not as stiff as expected and thus were modeled with a lower stiffness of 1E4 N/m also with 200 lbf (890 N) of initial force, which were also updated after the initial reads from load cells.

In the experiment, after welding and a given cooling time (<60 s), the component was removed from the fixture and placed aside. This process is represented in the model by a change in boundary conditions. Clamps and bearings are deactivated, and a 3–2-1 scheme takes place simultaneously. This is done to have minimal impact on both residual stress and resulting body distortion and to avoid rigid body movement. The manner of node fixation is depicted in Fig. 6. Figure 12 shows the final condition of the distortion at room temperature with components supported in the 3–2-1 condition.

Table 6 Chemical composition [wt %] of HR500LA

Al	C	Fe	Mn	Nb	P	S	Si	Ti
0.037	0.07	98.17	1.45	0.04	0.014	0.003	0.09	0.001

Figure 7 shows plots of material data used in this model first calculated using *JMatPro®* based on the chemical composition and as-received condition listed in Table 1. This data is then curated and fine-tuned based on available

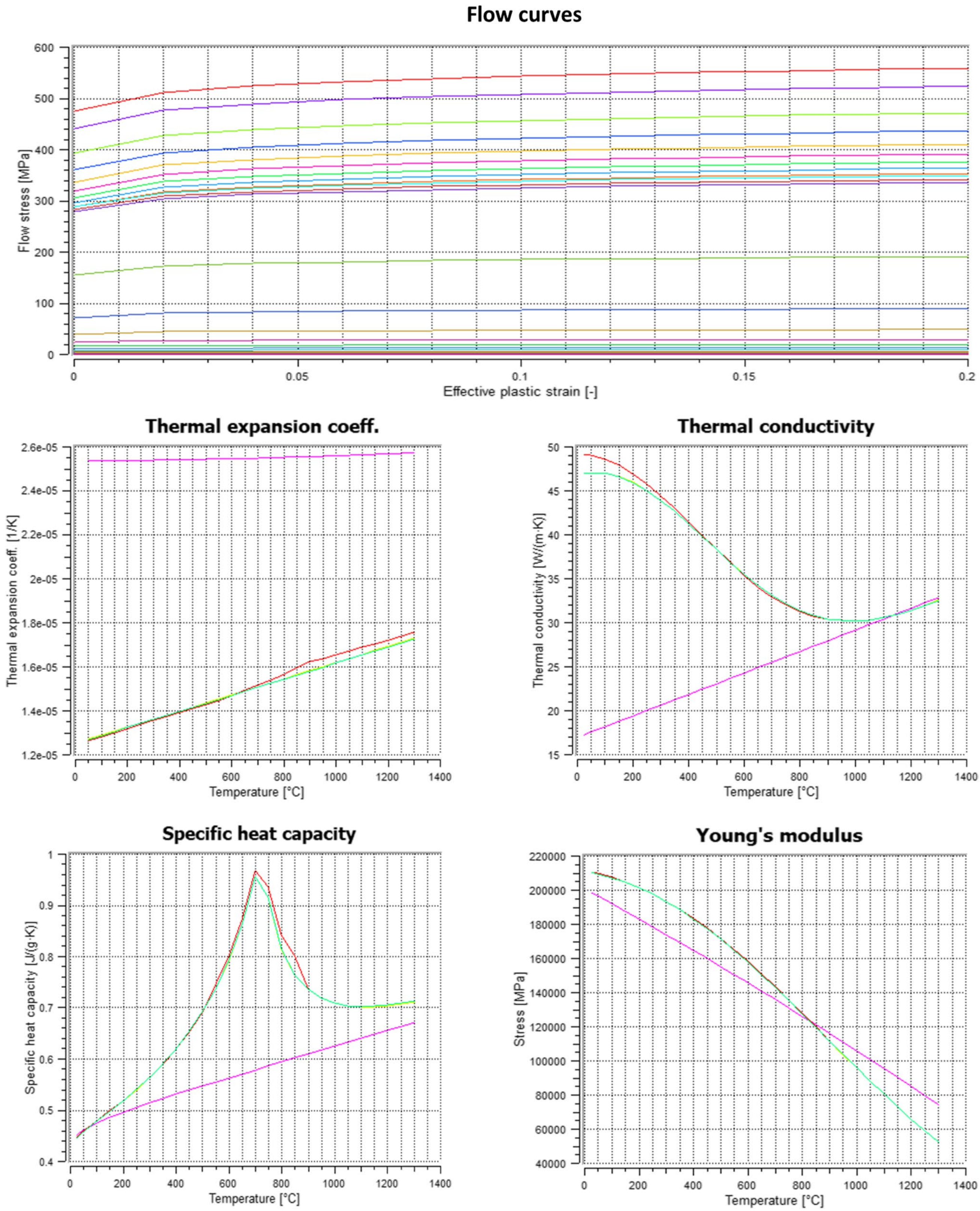

Fig. 22 Thermomechanical data from JMatPro® and curated using available tensile test data

characterization information like tensile tests, micrographs, and hardness measurement from public literature. This helps with adjusting coefficients and flow curves to better match the as-received (pre-weld and post-weld) responses. Phase transformation information is intentionally included in this analytical material calculation, strains inherently coming from crystallographic changes (FCC to BCT, FCC to BCC) are considered in the calculation as they are part of the total

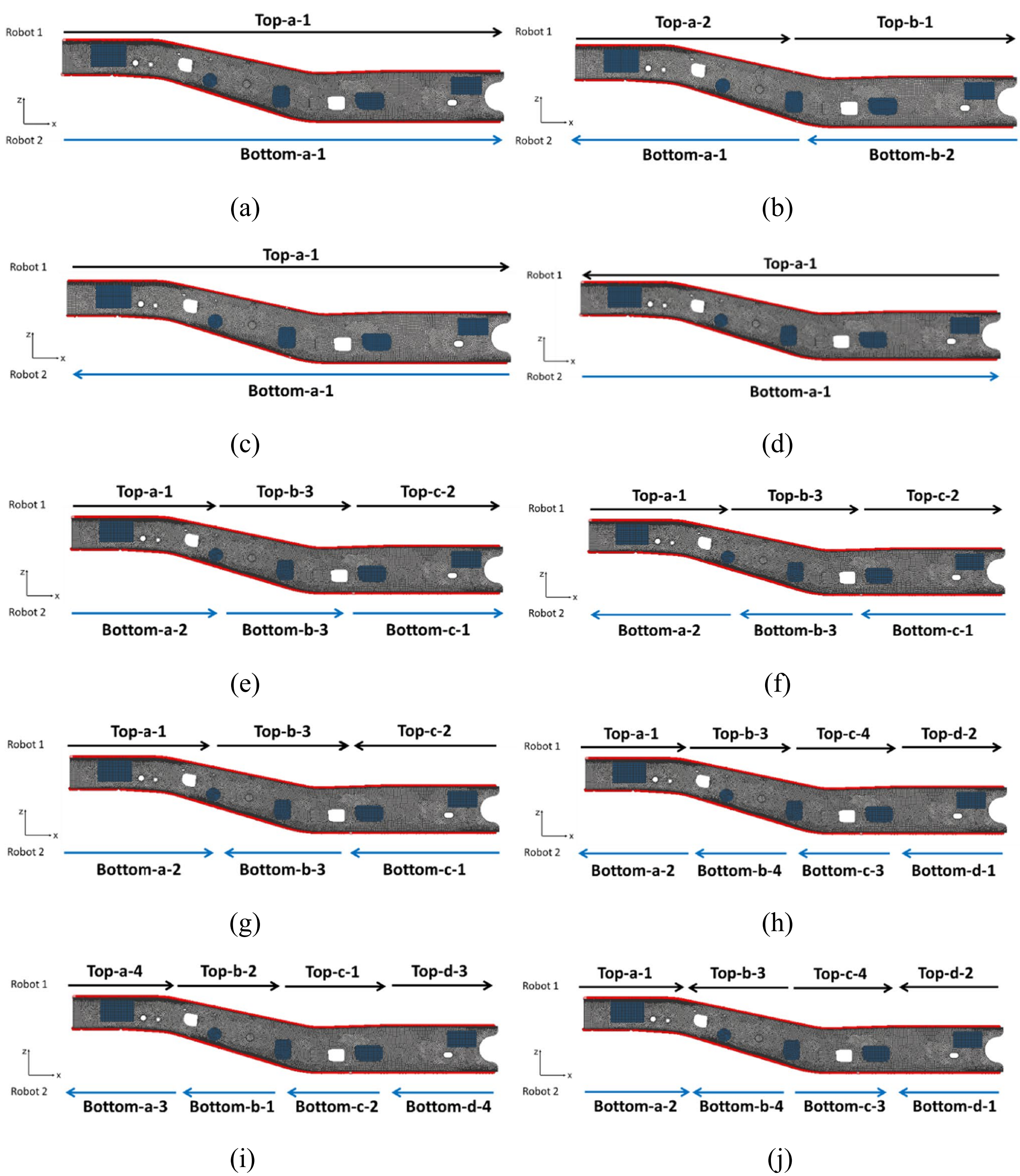

Fig. 23 Welding segments, sequence, and direction for case study

Fig. 24 Welding segments, sequence, and direction for case study

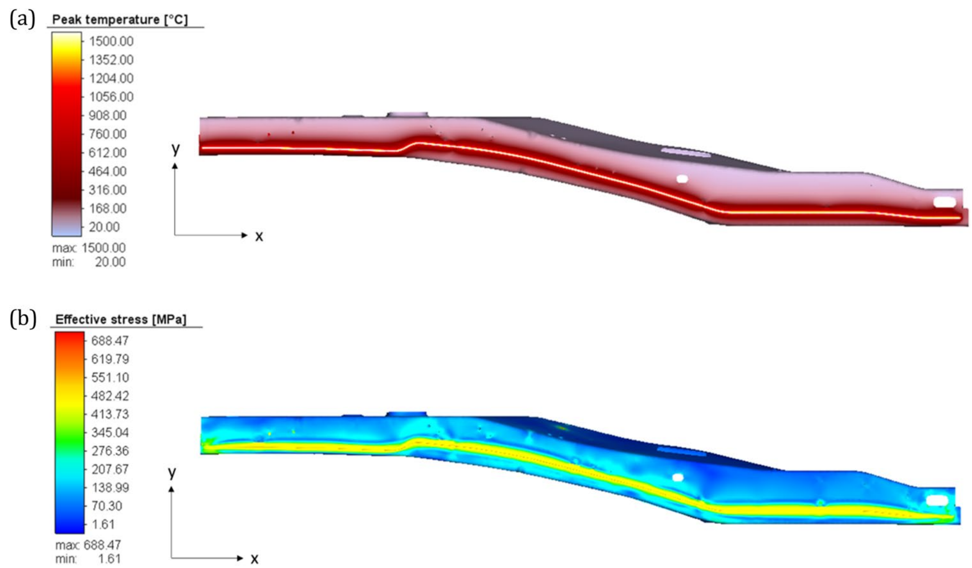

strain (elastic, plastic, thermal and metallurgical) via local volumetric expansion. Neither the various austenitization behaviors of individual initial phases nor the actual austenitization kinetics are accounted for. Instead, the austenite phase fraction is assumed to increase linearly between *Ac*1 and *Ac*3. Nevertheless, this linear austenitization model correctly reproduces the linear material expansion that is expected after austenitization. Hence, the model fully serves the purpose of efficient simulation of a complex process. The martensitic transformation model follows the Koistinen-Marburger to reproduce the martensite phase fraction during cooling. Thus, the expected linear expansion of the material sample is obtained at all temperatures as a combination of thermal, mechanical, and metallurgical effects. To validate this section of the material card, one should normally run a virtual dilatometric test and compare it with experimental data. The resulting mix of phases (as they happen) serves as a basis to update the flow stress of each node in the model. A multidimensional lookup table composes the thermomechanical response of the model as a function of temperature, strain rate, and calculated phase fraction at the nodal level. When more than one phase is present, a linear mixing rule is applied. If a certain portion of the model containing stress is reheated, that stress condition will be updated using a different flow curve suitable for the temperature and actual phase fraction. Hardening coming from previous phases is part of the history of the model as early increments; when temperature is increased by the heat source, the allowed stress is lower than the existing stress; annealing takes place as the material gets softer.

For heat transfer analysis, all bodies are assumed to be initially at room temperature, defined as 20 °C, and the heat transfer coefficients of the material are used as listed in Table 3.

Weld trajectories are defined as a point sequence, and these can be defined by picking locations directly in the GUI or by providing a suitable CSV file with coordinates and torch orientation vector. Trajectories can then be reordered, replaced, split, reversed, or positioned like any other object in the model view window. For the multiple experimental tests, the only change needed was trajectory reversal for some of them. Tack welds can be added using the same mesh as the weld beads thus avoiding overlapping elements. As described previously, elements in a weld bead are only activated based on temperature.

What represents the heat coming from the power source (torch, laser beam, electron beam, etc.) is modeled as a volumetric heat flux. For arc welding processes, this heat source is based on the Goldak [29] geometrical definition of a double ellipsoid. The heat source needs to then be thermally calibrated to have the correct/expected weld penetration profile which depends on multiple factors: heat input, travel speed, and the volumetric definition. For this model, the process parameters are provided by Table 2 and Table 4. Important to notice, the provided values do not come from analytical estimations but rather

Table 7 Distortion results based on maximum total displacement

Case	1	2	3	4	5	6	7	8	9	10
Distortion [mm]	15.85	14.39	9.68	11.95	13.64	15.16	8.76	13.89	12.95	13.20

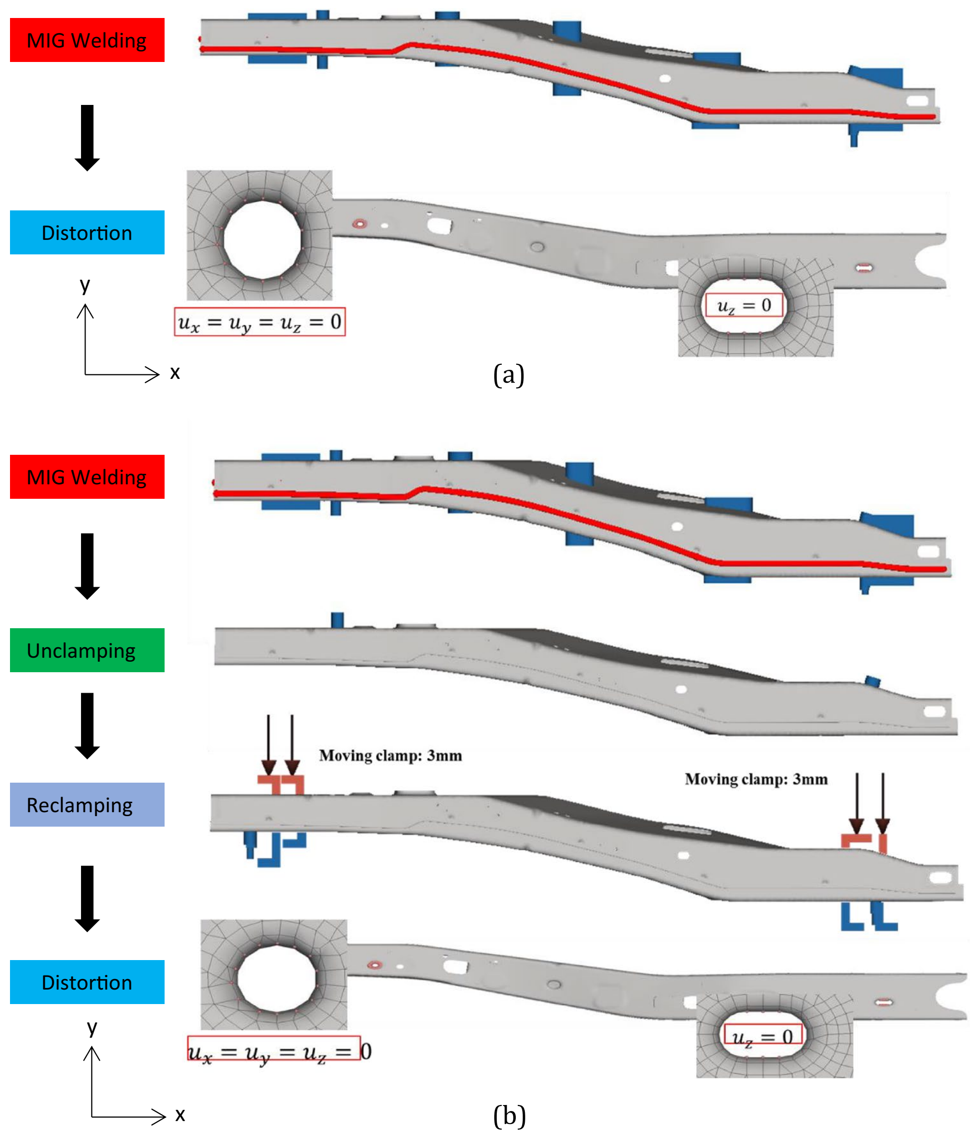

Fig. 25 Welding processes: trial process (a) and optimum process (b)

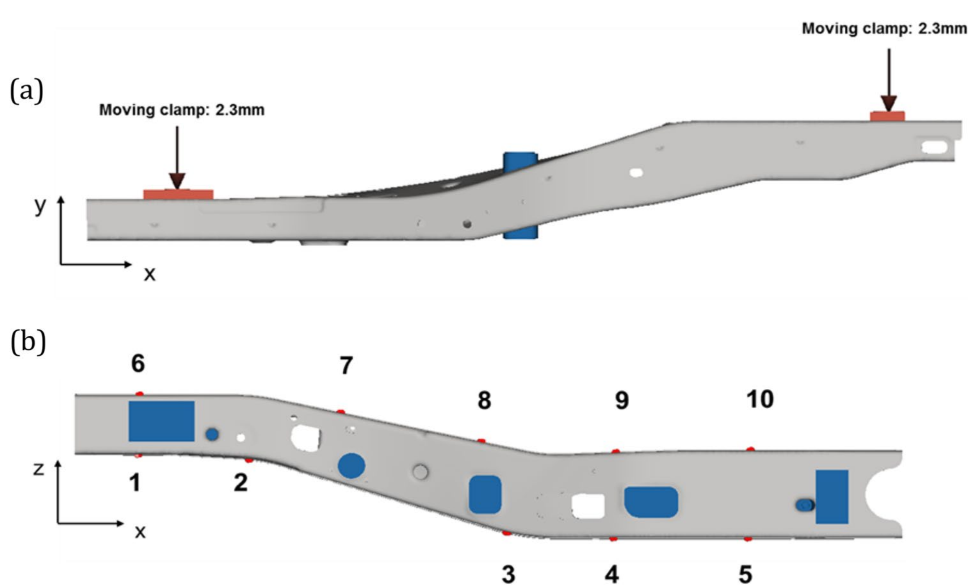

Fig. 26 Fixturing condition: prebending (a) and fully clamped for welding (b)

Table 8 Heat source parameters for tack welding

Voltage (V)	22.0
Current (A)	200.0
Speed (mm/s)	16.7
Efficiency	0.8
Conical heat source upper radius (mm)	1.5
Conical heat source lower radius (mm)	1.5
Conical heat source depth (mm)	3.0
Gaussian parameter	3.0
Volume heat fraction	1.0
Surface heat source disk radius (mm)	0.0
Surface heat source depth (mm)	0.0
Heat front scaling factor	0.4

from experimental validation data downloaded from the welding power source.

2.3 Validation with temperature distribution

Accurate prediction of temperature gradients in the assembly during welding is the critical step for numerical simulation of thermal distortion. Figure 8 is a time series of images of temperature distribution simulated as welding progresses for cases 1 and 2. The welding and cooling times for case 1 are each 48.8 s (open arc) and 527 s; and 52.5 s and 527 s seconds for case 2 which includes the tack welding sequence. In order to validate the temperature distribution predicted by the numerical simulation with the actual welding test, 12 reference points were selected on the assembly (refer to Fig. 9 to note the thermocouple placement (labeled as TC01 through TC12) on the lower and upper channels for temperature measurement). The precise coordinates for each thermocouple were acquired from the scanned image of the channels. Note that welding path 1 begins from the end near thermocouples TC07 and TC10 and welding path 2 begins after a 1-s time delay from the opposite end near TC03 and TC06.

The transient temperature distribution obtained from the numerical simulation is compared with the measured data, refer to Fig. 10 for case 1 and Fig. 11 for case 2. It can be observed that the temperature histories predicted by the simulation are in excellent agreement overall with the measured temperatures at the 12 probe locations for both cases 1 and 2.

2.4 Validation with displacement distribution

Large temperature gradients during welding introduce assembly distortion after welding. Figure 12 is a series of images presenting the total displacement fields due to

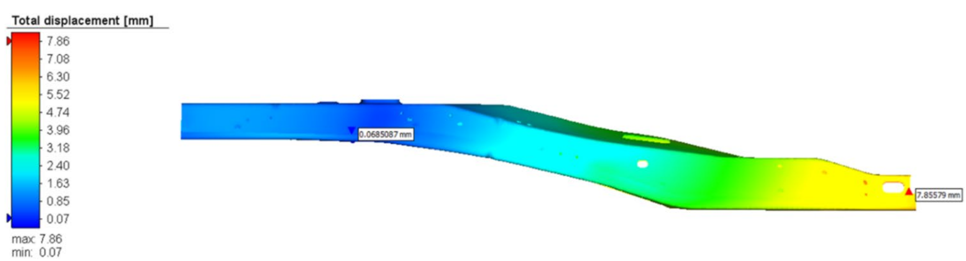

Fig. 27 Simulated distortion with pre-bending followed by tack welding and optimal process

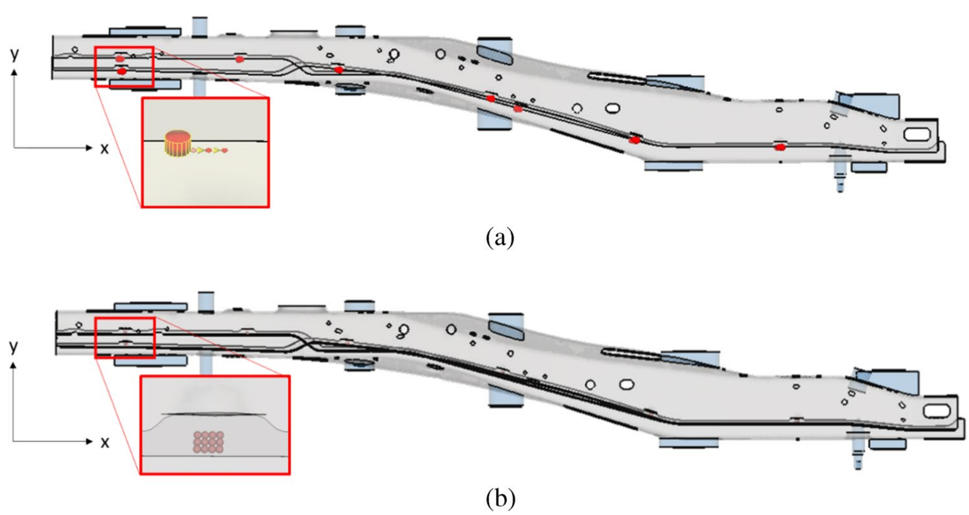

Fig. 28 Simulation model for tack welding with heat source (a) and local joints (b)

thermal distortion of the straight-clamshell after welding as predicted for cases 1 and 2. For case 1, refer to Fig. 13a, relatively large deformations (~ 8 mm) can be observed near the upper channel corners where the welding terminates, whereas very small or almost no deformation can be observed in the lower channel especially near the clamping areas. For case 2, the deformations in the upper channel are larger near the edges compared to those in case 1, which can be expected as the upper and lower channels are tack welded before welding and the upper channel is not clamped during welding. The maximum distortion location and its magnitude (~ 1.5 mm) predicted by simulation matches are found to match very well with actual welding test measurements for both cases 1 and 2.

To validate the numerical simulation results with the actual welding test data, the displacement distribution over the entire assembly predicted by the numerical model was further validated by comparing it with the 3D scan data of the assembly. The distortion of the assembly after welding was measured by the Hexagon 3D imaging laser scanner as follows. Firstly, the upper and lower channels of the assembly were scanned before welding—let us denote this pre-weld image (or point cloud which is a dataset of Cartesian coordinates of points representing the shape of the channels) as $\Phi(x, y, z)$. After welding, the assembly was scanned using

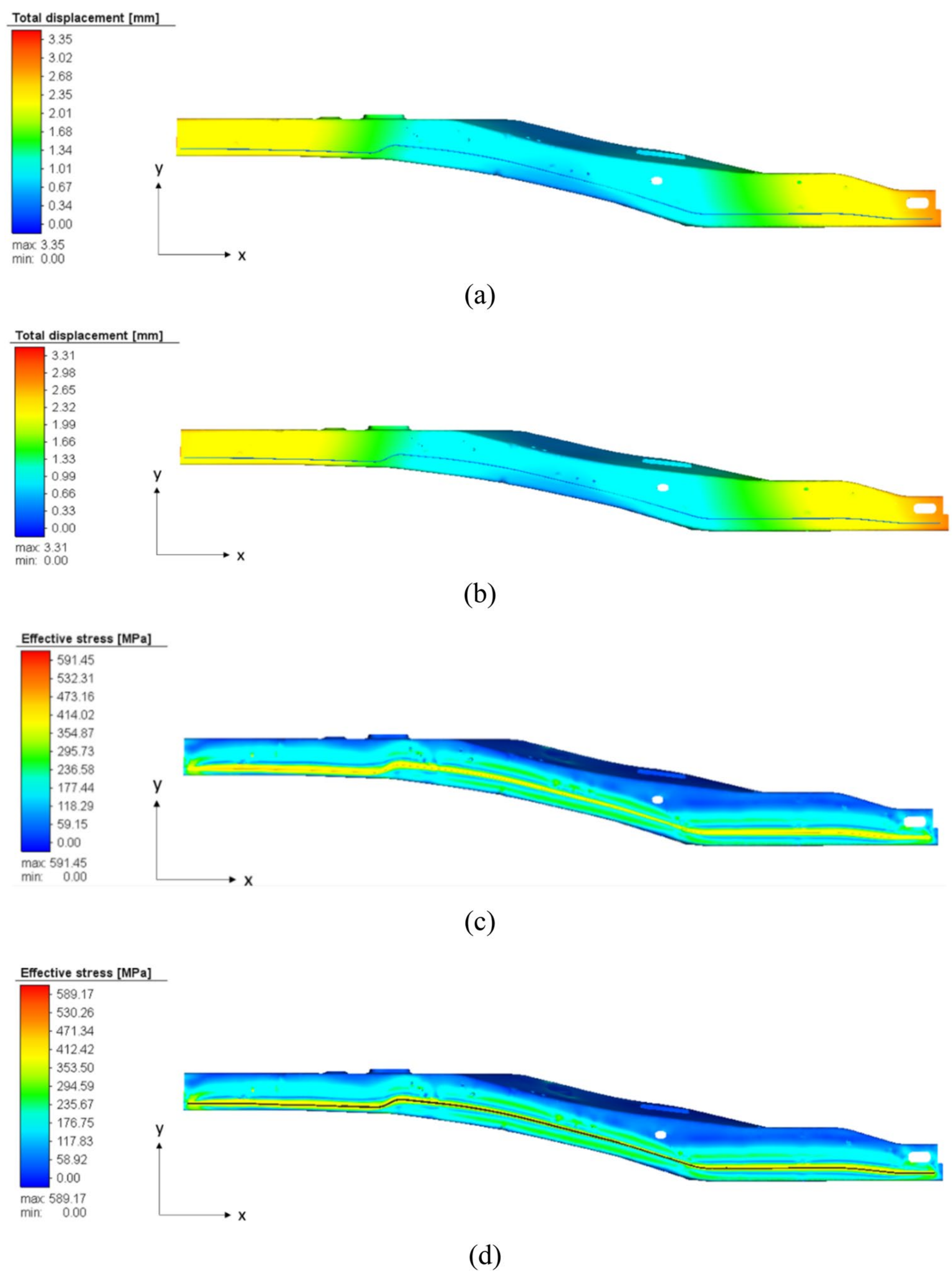

Fig. 29 Simulation results: displacement after welding with tack welding using a heat source (a), displacement after welding with local joints (b), effective stress with tack welding using a heat source (c), and effective stress with local joints (d)

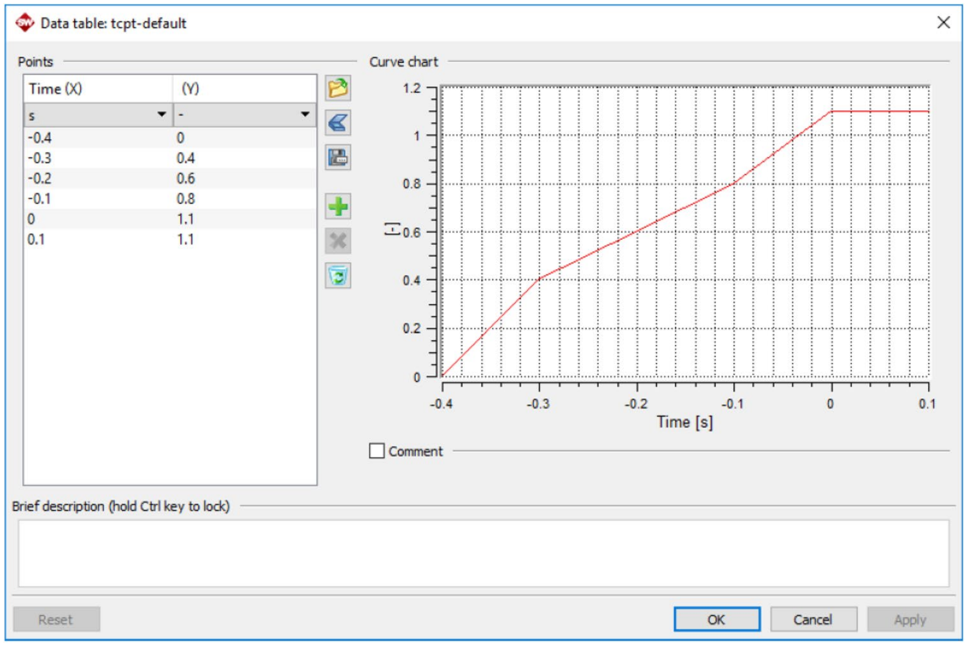

Fig. 30 Default thermal cycle table

the same scanner—let us denote this post-welding image as $\Phi^{'}(x, y, z)$. It follows then that $\Delta\Phi = \Phi^{'} - \Phi$ would be the point cloud representing the true displacement distribution due to distortion induced by welding. Next, the point cloud $\Delta\Phi$ was imported and then aligned to the straight-clamshell CAD model using the Best Fit algorithm. Figure 14 is an image of the overlayed and aligned point clouds of simulation and CAD model of the "straight-clamshell" for case 1. The displacement field obtained from the simulation was also imported and aligned to the CAD model in the same manner. Presented in Fig. 15a is the comparison of distortion predicted and the scanned image for case 1, where the color map represents the displacement normal to the surface of the assembly before welding. The two results are in excellent agreement. Figure 15 b for case 2 also exhibits a good agreement between the two results.

The comparisons made in Fig. 15a, b are using data from experiment and simulation in the post-weld condition, room temperature and supported by the 3–2-1 restraints to minimally influence the distortion. By comparing directly

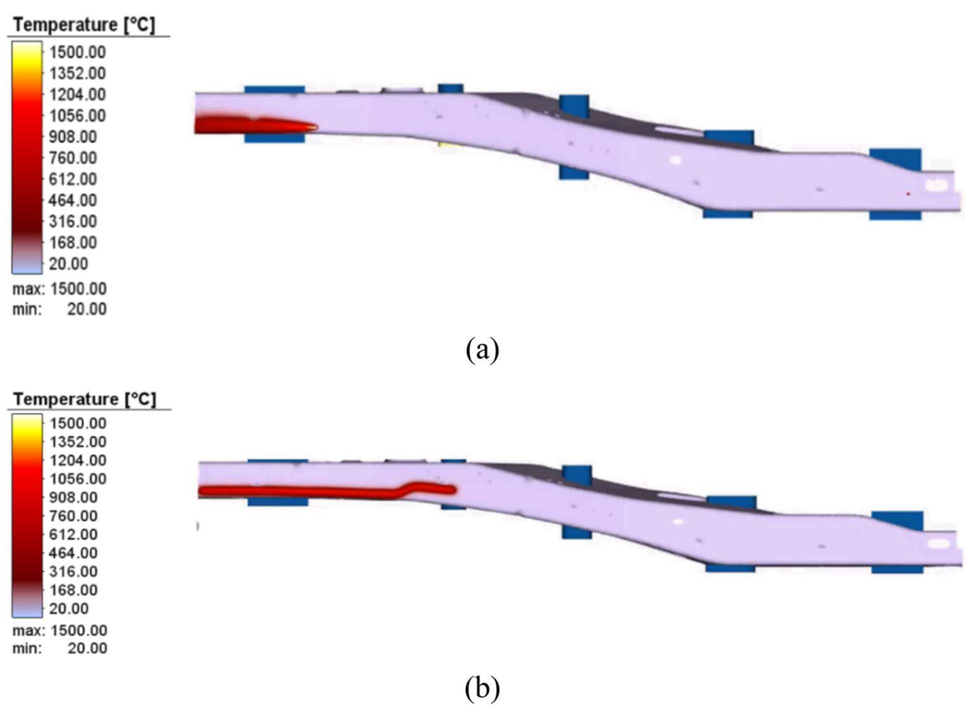

Fig. 31 Temperature distribution by transient simulation (a) and thermal cycle simulation (b)

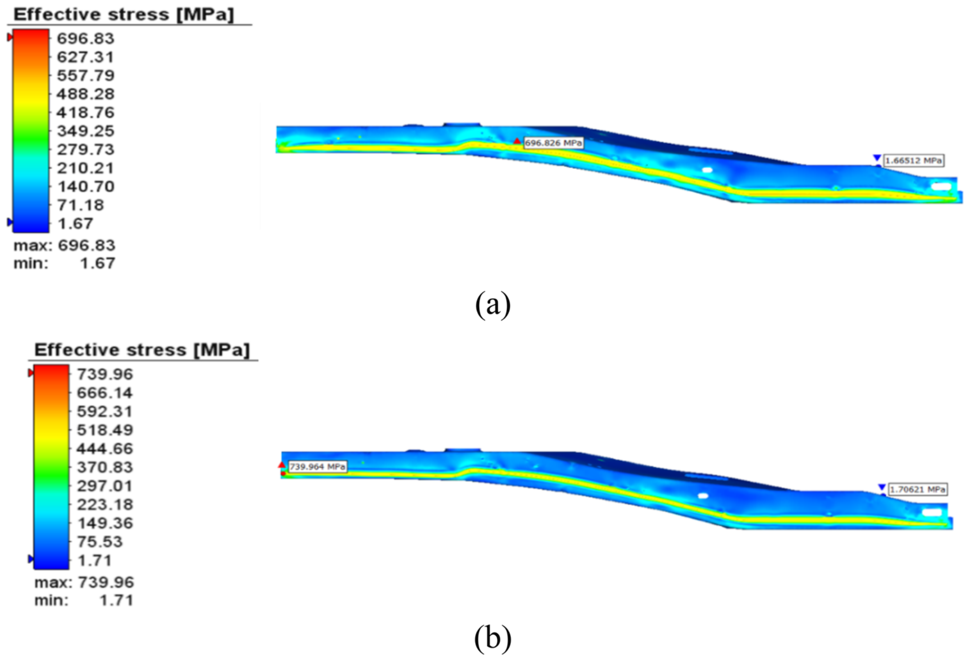

Fig. 32 Effective stress distribution by transient simulation (a) and thermal cycle simulation (b)

to CAD, it is possible to do a qualitative and quantitative assessment of the simulation accuracy when looking at the same comparison between the experiment and CAD. This means simulation-to-CAD is a "what results would I get if I weld it this way," while "experiment-to-CAD" means "what did I get compared to nominal shape." It is also possible to compare simulation to experiment and it is done this way for the truck rail in a later section (see Fig. 43).

2.5 Validation with load cell measurements

The aluminum frame supporting the top clamps was bent during preliminary tests and replaced with a steel frame, which indicated large clamping forces due to distortion of the assembly were generated during welding. The clamping forces due to distortion were also measured using the load cells during welding in order to validate the distortion predicted by the numerical model.

Figure 16 identifies the probe locations of 8 load cells. The reaction forces on the sides of the lower channel were measured by 6 load cells and those on the top of the upper channel were measured by 2 load cells attached to the top clamps. Figure 17 presents the comparison of clamping forces due to distortion between the test and simulation data for case 1. Note that the readings from the load cells (LC04 and LC05) affixed to the upper channel surface are

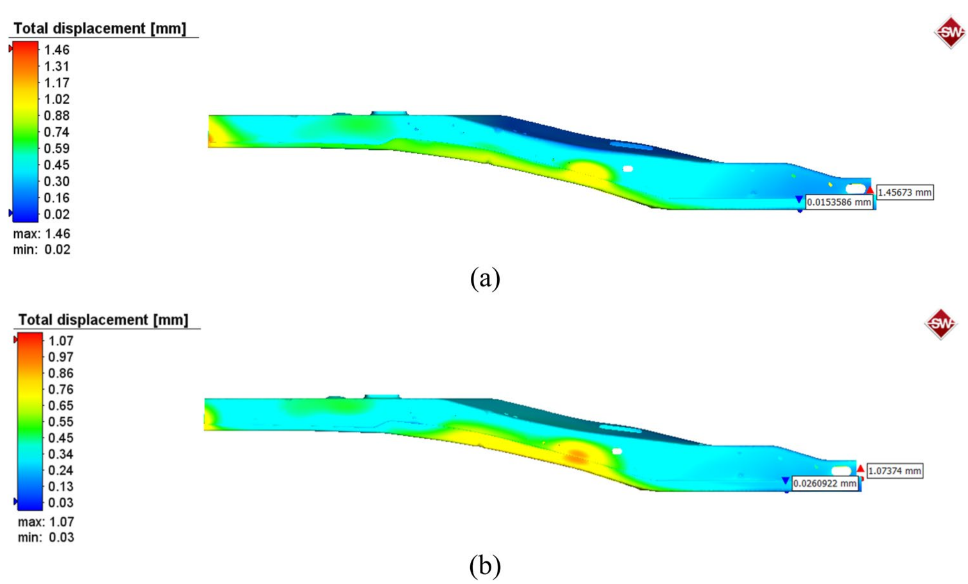

Fig. 33 Displacement distribution by transient simulation (a) and thermal cycle simulation (b)

not presented in the graph as their values were negligible because the clamps supporting the load cells were not stiff enough. Based upon the plots in Fig. 17 it can be concluded that the predicted reaction forces by the numerical model agree very well with the actual measurements.

2.6 Validation with weld penetration

Figure 18 is a series of photomicrographs of the actual welds on the straight-clamshell assembly for Cases 1 and 2. Figure 19 includes two images of the weld penetration simulation for comparison. In the macrographs there is some undercut happening at the flat surface and the edge of the straight part has been consumed by the weld. When calibrating the heat source for the welding simulation, one usually does not want to have any undercut condition. This is one of the most important steps when performing welding simulation as the result of the thermal input and heat distribution will dictate the response of the structure (distortion and stress); therefore, special care must be taken to properly capture the welding process. The simulation will keep a smooth cross-section throughout the weld bead unless a variation of it is desired. In this study, the weld was performed by two robots and parts were fixed in a rigid fixture, which is a very stable condition. Despite not reflecting all the variations in the macrograph, the weld effect in the simulation model was accurately captured.

3 Truck rail GMAW simulations

The capabilities of the FEA software for welding distortion prediction were further evaluated through the simulation of production level truck rails GMAW under various process conditions such as clamping-unclamping process design, pre-bending and tack welding, the number of weld segments, welding sequence, and direction. Through this evaluation study, the effects of infinite heat sink, preheating of components, thermal cycle (or meta transient) boundary conditions, local joints, and contact behavior of the boundary conditions on welding distortion were investigated.

3.1 Tryout welding simulations

Figure 20 is an image of the simulation model, where the gray, blue, and red parts each represent the upper and lower frame rail parts, fixture, and robot welding paths. Each rail part was modeled with hexahedron-type elements with a 2-mm average length near the welding area and a 6-mm average length for the area far from the welding area. With two layers through the thickness, 73,164 and 69,522 elements were constructed for the upper and lower components, respectively. The eight points Gaussian integration method was used for the elements. Fixtures were modeled as a bearing boundary condition (rigid body) and the calibrated welding parameters such as velocity, current, voltage, and Goldak's parameter are listed in Table 5.

Figure 21 presents images of the simulated weld penetration when applying the calibrated parameters. Total welding time is approximately 106 s for both welding paths and the weld parts are cooled down for 354 s. After the welding and cooling simulation, the distortion prediction was successively conducted. For material properties, HR500LA was calculated using JMatPro® and used for the simulation. The heat transfer coefficients of the material are the same as those listed in Table 3 and the chemical composition is listed in Table 6. Figure 22 are plots of the thermomechanical properties used for the truck rail.

3.2 Effects of weld segments, sequence, and direction

Case studies with a different number of weld segments, sequences, and directions were performed and a total of 10 cases were constructed, refer to Fig. 23, where the arrow and number on the arrow indicate welding direction and sequence, respectively. Figure 24 a presents the peak temperature distribution and Fig. 24b the residual stresses (effective stress component) induced by the welding process for case 7. The contour results for other cases are nearly identical with those for case 7. The predicted distortion for all the cases, which is based on the maximum total displacement value in the simulation results in the unclamped condition back at room temperature, are listed in Table 7. As listed in Table 7, the minimum distortion is predicted for case 7 and represents a 45% decrease in distortion compared to the maximum distortion case (case 1).

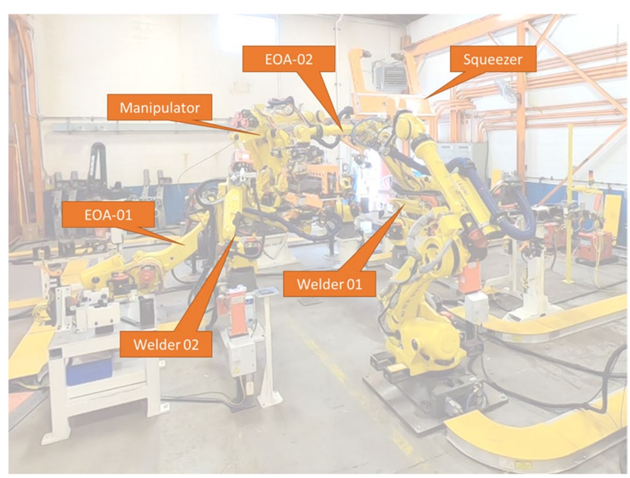

Fig. 34 Welding test setup for truck rail

3.3 Effects of clamping and unclamping

The effect of the clamping-unclamping process upon distortion was identified by simulation. The two different clamping-unclamping processes for welding and cooling are detailed in Fig. 25. For the first design, both welding and cooling are conducted with the same fixture as indicated in Fig. 25a. However, for the second design, refer to Fig. 25b, welding and cooling were performed with different fixtures which introduce additional processes: unclamping for 5 s and re-clamping for the cooling process with a duration of 600 s. The second process, called the optimum process hereafter, exhibited a 21% decrease in distortion compared to the first process called hereafter the trial process. With the optimum process, the effect of pre-bending followed by tack welding on the distortion was simulated. Figure 26 a details the pre-bending process before welding. Two fixtures are located at the center and modeled as a bearing boundary condition. Two moving clamps are located at both sides and move to the pre-defined direction about 5 mm in

Fig. 35 CAD model for truck rail welding fixture

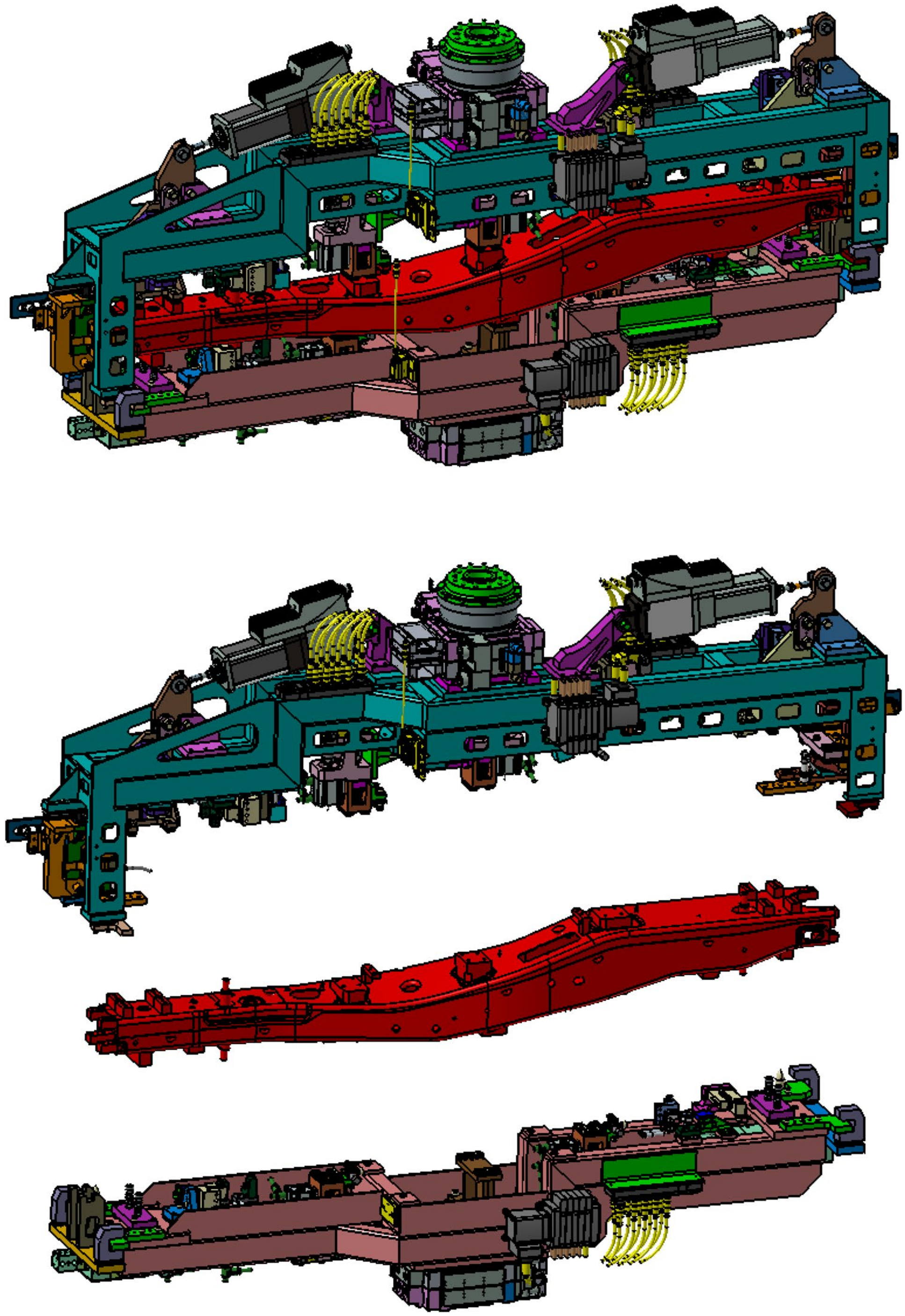

Fig. 36 3–2-1 locating scheme

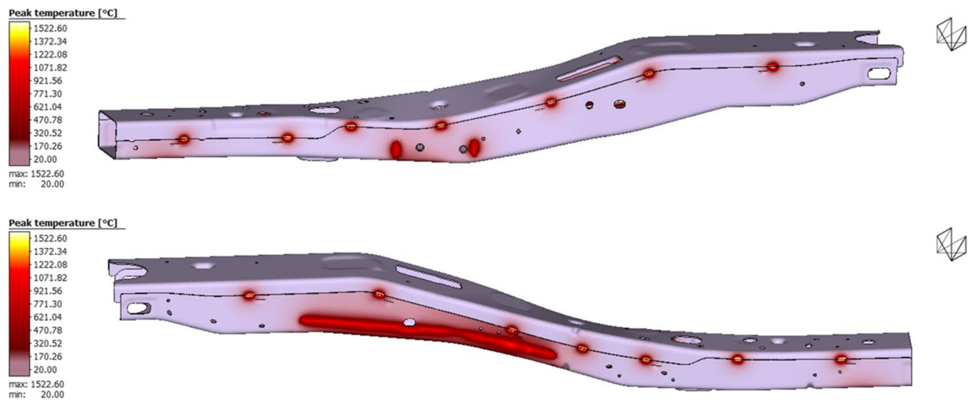

Fig. 37 Tack weld locations

5 s. The remaining processes for welding and cooling are the same as for the optimum process. After pre-bending, tack welding before gas metal arc welding was modeled, refer to Fig. 26b, where tack welding is applied to the ten points and the number at the points indicates the sequence of tack welding. The heat input and cylindrical heat source model's parameters are listed in Table 8. The optimum process with pre-bending followed by tack welding exhibits a 42% decrease in distortion compared to the trial process as indicated in Fig. 27.

3.4 Effects of tack welds

To investigate the effects of tack welds, local mesh connections were used in comparison with simulating a full thermo-mechanical tack welding process. The mesh connections (via local joint boundary conditions) were applied to the area for tack welding with a size of 8 mm × 6 mm, refer to Fig. 28. In addition, Fig. 29 are contour plots of the distortion and effective stress for the two cases. Considering that simulation time with the local joints is approximately 23 h which is 5 h faster than the simulation using tack welding as a heat

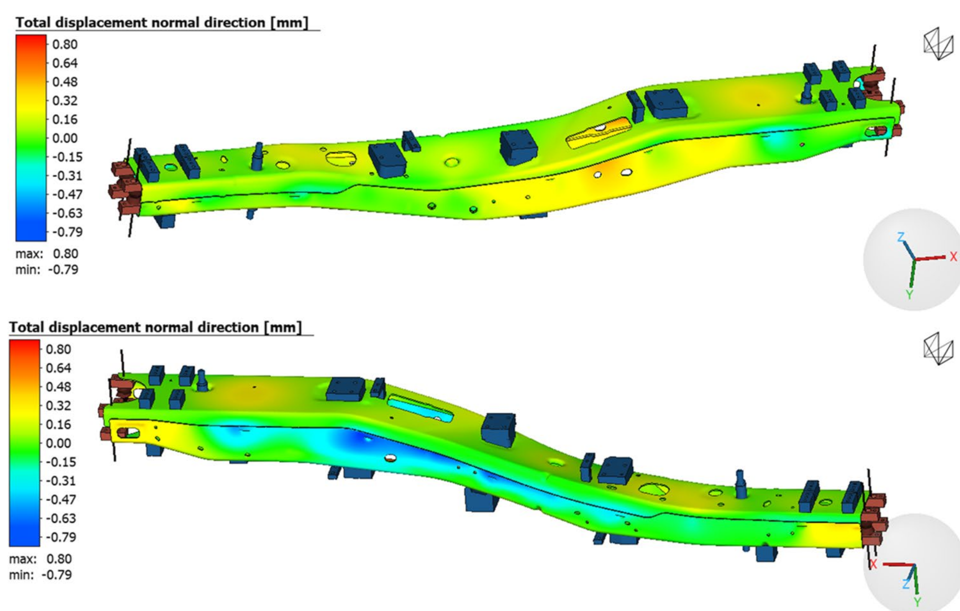

Fig. 38 Displacement distribution after tack welding

Fig. 39 Stress distribution after tack welding

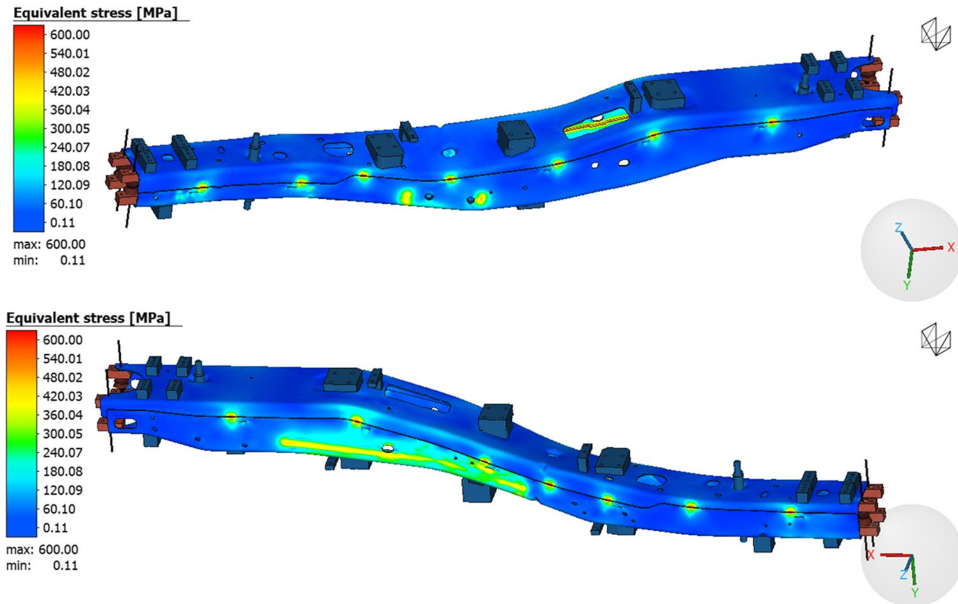

Fig. 40 Full welding simulation model

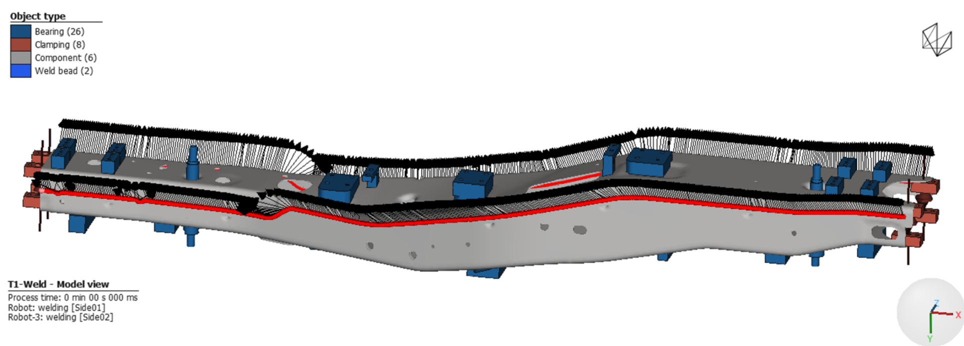

source, it would be efficient to use the local joint boundary conditions instead of using a heat source for tack welding.

3.5 Effects of thermal cycle boundary conditions

It is well known that the accuracy of the simulation depends on the number of elements though using a greater number of finite elements for improved accuracy requires a lengthy computation time. The software provides a thermal cycle (or meta transient) simulation in which the heat source is replaced with thermal boundary conditions. In transient simulation, which is the method mainly discussed up to this point, the heat source moves along the weld seam and the temperatures of the elements located at weld seams are calculated based on the heat transfer equation and heat source. For thermal boundary conditions, such calculations are not required, and the temperature boundary conditions are directly applied to (in a simplest case) the entire length of the weld seam. Hence, the local effects of heat over time and their consequences for the total structure are calculated. On the other hand, the model setup of the thermal cycle simulation is based on the transient simulation. Instead of defining an energy input, a time–temperature look-up table is defined, refer to Fig. 30, where the origin of the horizontal axis is the time when the heat source reaches the mid position of the weld path in a transient process and thus negative values can be defined. The temperature axis describes a unitless relative temperature. The value 0 defines the room temperature and 1 the melting temperature. Note that it is possible to define the values up to 2. The thermal cycle table should always start at room temperature, i.e., the relative temperature of 0. As presented in Fig. 31, the heat source reaches the mid position of the weld seam in the transient simulation, while the temperature boundary conditions are

Table 9 Welding timing table

Trajectory	Start (s)	End (s)
R1-1	0.0	53.3
R2-1	0.0	55.51
R2-2	58.0	109.9
R2-3	111.3	163.7

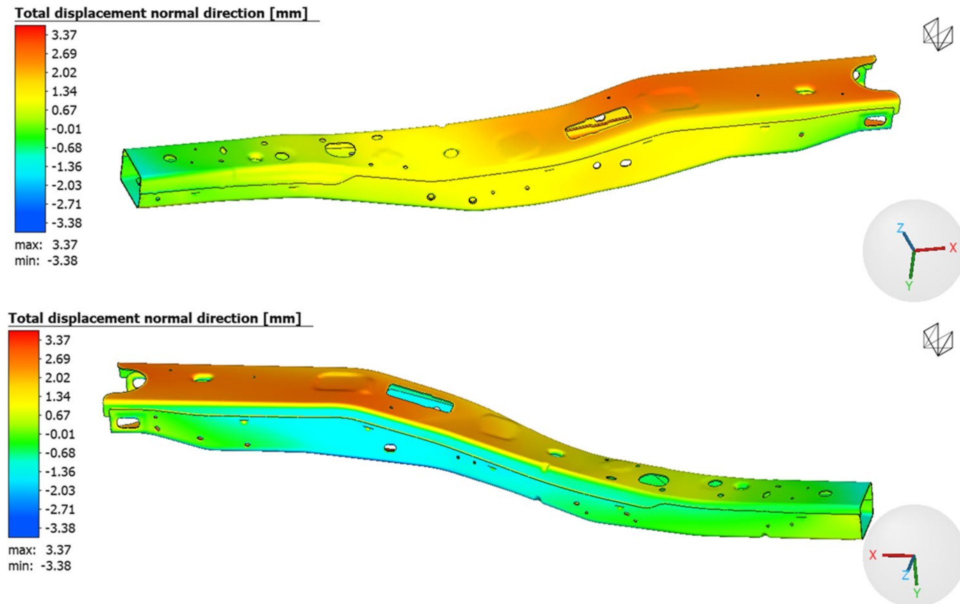

Fig. 41 Displacement distribution

applied to the entire weld seam in the thermal cycle simulation. The simulation results present the apparent difference in terms of magnitude, but the tendency appears to be similar between the transient and the thermal cycle simulation, refer to Fig. 32, for the effective stress distribution and Fig. 33 for the displacement distribution. Considering that the thermal cycle simulation requires approximately 5 h for computation with the GM high-performance computer, which is 10 times faster than the transient simulation, it is worthwhile to consider the thermal cycle simulation for the optimization of welding parameters that requires significant computational time.

3.6 Modeling the tryout welding conditions

To reproduce the tryout welding conditions as close as possible, the CAD model of the real fixture, refer to Fig. 34, and recorded process timing were utilized. The baseline truck rail model was then updated, and the same analysis was performed. For welding simulation purposes, the only part of the fixture that is relevant is the contacting bodies. Therefore, using an automated tool in Apex, the fixture was segregated and only the clamping blocks, pins, and net pads that were directly in contact with the rail were considered. This reduces the calculation time considerably as those are the only expected contact pairs to be updated.

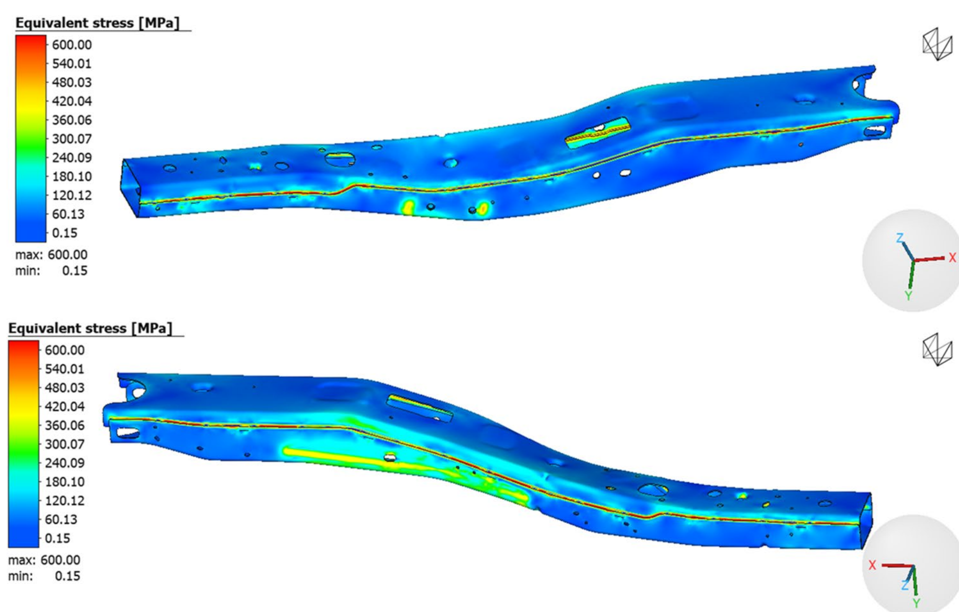

Fig. 42 Stress distribution

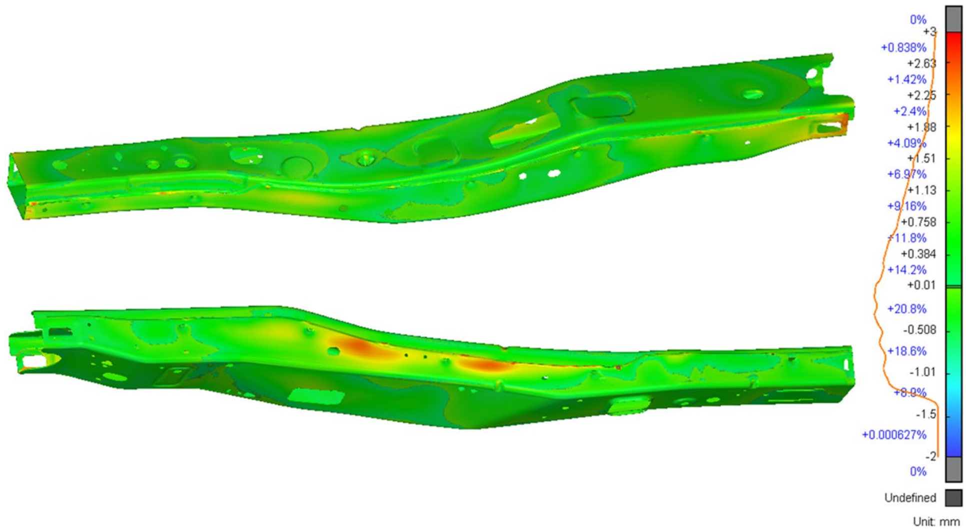

Fig. 43 Comparison of displacement distribution with scanned image

For the simulation model, there is an initial contact calculation based on specified tolerance. If a body is found not to be within that tolerance to any other body, the solver automatically removes that body from the model in the first increment. Figure 35 is a model of the rail, colored in red, and fixture blocks considered in the simulation. The other components were disregarded. As explained in the straight-clamshell model in Sect. 2.2, bearings and net pads have infinite stiffness and do not react to forces. Clamps in this truck rail model have 10^6 N/m stiffness and apply 200 lbf of force.

For the post-weld completion, the part needs to be free from the fixture so in its final shape it can be measured and compared with the experimental results. For that, a 3–2-1 locating scheme illustrated in Fig. 36 was applied. The 4-way pin locks all three translations, and the 2-way pin locks the side movement. This is also to avoid rigid body motion and guide the best-fit method once the scan data is overlaid onto the simulation results for surface deviation calculation. After the clamps grab both halves of the rail, the parts are held in a fixtureless condition. With the help of a squeezer tool, two welding robots then tack weld them together simultaneously at the location of the louvers and at intermediate locations, refer to Fig. 37.

Tacking is a process that should not cause excessive local distortion. Combined with the squeezer, the model was able to predict the distortion before performing the full weld. Figure 38 are images of the surface deviation of the tacked condition. A positive value indicates distortion in the same direction as the normal area vector, while a negative value indicates the opposite. Stress condition is also important since the tack weld should not break during the welding process. Figure 39 presents the von Mises stress distribution in the post-tacking condition. Immediately following the tack welding, full welding simulation, refer to Fig. 40, is performed. Weld beads are modeled to cover the entire thickness of one side of the joint with both legs of equivalent length. The torch angle is kept at 45° from the sides to provide more evenly distributed heat. Weld sequence and timing between trajectories are done as specified in Table 9.

After performing the welding simulation, the part is set at rest at the 3–2-1 points for measurement and comparison with experimental data. Figure 41 presents the surface deviation of the simulation only.

This surface deviation does not reflect the best-fit condition between the CAD and simulation results, this result is to compare how much the part deviates in terms of direction. As a means of comparison with the tacked condition, stress plots in Fig. 42 present a greater stress level because of the added welds.

To validate all the assumptions and results of the welding model, a shape comparison calculation was done using Hexagon's 3DReshaper. Figure 43 is a contour plot of the dimensional difference between the simulation versus the scanned part shape. One can see that the parts align very well which serves as proof that welding simulation, when done properly, can be used as a predictive tool. The few red spots along the seam weld are attributed to the extra material added by the tack welds. In the simulation this is treated as a single mesh, therefore no 'bump' in the weld bead is produced. In the second image of Fig. 43, the yellow and red areas indicate that part fit-up is not good in those regions or squeezing force prior to tacking caused excessive distortion. These are localized distortions which require further investigation.

4 Conclusions

This paper details finite element methods and simulation procedure of predicting welding-induced distortion during GMAW of HSLA steel components in automotive body assembly. Two case studies were presented, i.e., straight clamshell and truck rail assemblies. Simulation results were validated with various measurements, all showing excellent agreements.

1.For the straight-clamshell assembly:

•Simulations of transient temperature gradient due to heat input under various welding sequences matched very well with thermocouple measurements in terms of both the peak temperature and the overall heating and cooling temperature history.
•Simulation results were also compared with the clamping forces measured using load cells during welding tests. A very good agreement between simulation and test data was found.
•The simulated distortions of the assembly under various welding conditions all showed more than 95% of correlation with the laser scanned (i.e., measured) dimensions.
•Welding distortion is greatly affected by tack welds. Without tack welds, the maximum distortion was found to be more than 8 mm at one location, whereas the distortion was reduced to about 2 mm with properly placed tack welds.

2.For the truck rail assembly:

- A total of 10 different experimental welding conditions were simulated, followed by a comparative study to determine the impact of weld sequence on assembly distortions.
- The simulated distortions matched measurement data very well except for a few local points, mostly at the tack weld locations. A maximum 0.9-mm deviation of the rail surface was observed when comparing the simulated results to the scanned data of the actual welded assembly.

The following are found to be the key lessons learned for accurate welding distortion simulations:

- Use fully coupled thermal-structural finite element analysis with solid elements;
- Accurate material data, including temperature-dependent thermo-physical properties (e.g., heat capacity) and mechanical properties (such as the flow stresses), are critical to the simulation accuracy;
- Phase transformation has to be considered in the simulation since it causes both volume changes and mechanical property changes, particularly during the solidification stage;
- Adaptive activation of the weld elements is a must for accurate predation;
- Various geometry and thermal contact conditions (between workpieces, as well as between the workpieces and adaptively activated weld elements) have to be included in the models.

This work provides a better understanding of the modeling and simulation capability of FEA for the prediction of welding-induced distortion and can be used as a guideline for accurate simulation of welding processes. The results indicate that FEA can be used with confidence to evaluate and mitigate weld-induced distortion during the design phase far in advance of production.

Acknowledgements The authors gratefully acknowledge Andrew Galant and Nathan Thompson for their assistance in instrumentation for the welding experiments and Aaron Steele for providing software and hardware support with the laser scanner and point cloud processing.

Declarations

Conflict of interest The authors declare no competing interests.

References

1. Ueda Y, Yamakawa T (1971) Analysis of thermal elastic-plastic stress and strain during welding by finite element method. Trans Jpn Weld Soc 2(2):186–196
2. Hibbit HD, Marcal PV (1973) A numerical, thermo-mechanical model for the welding and subsequent loading of a fabricated structure. Comput Struct 3:1145–1174
3. Lindgren LE (2001) Finite element modelling and simulation of welding – Part 1: Increased complexity. J Therm Stresses 24:141–192
4. Lindgren LE (2001) Finite element modelling and simulation of welding – Part 2: Improved material modelling. J Therm Stresses 24:195–231
5. Lindgren LE (2001) Finite element modelling and simulation of welding – Part 3: Efficiency and integration. J Therm Stresses 24:305–334
6. Michaleris P, Debiccari A (1997) Prediction of welding distortion. Wel Res Suppl 76:172–181
7. Michaleris P, Zhang L, Bhide SR, Marugabandhu P (2006) Evaluation of 2D, 3D and applied plastic strain methods for predicting buckling welding distortion and residual stress. Sci Technol Weld Join 11(6):707–716
8. Tsai CL, Park SC, Cheng WT (1999) "Welding distortion of a thin-plate panel structure. Weld Jo 78:156-s
9. Yang YP, Dong P (2012) Buckling distortions and mitigation techniques for thin-section structures. J Mater Eng Perform 21(2):153–160
10. Huang H, Murakawa H (2013) Development of dynamic mesh refining method for large scale thermal and mechanical analysis in welding and line heating. Trans Jwri 42(1):63–70
11. Huang H, Ma N, Murakawa H, Feng Z (2019) A dual-mesh method for efficient thermal stress analysis of large-scale welded structures. Int J Adv Manuf Technol 103:769–780

12 Lindgren L, Karlsson L (1988) “Deformation and stresses in welding of shell structures,.” Int J Numer Meth Eng 25:635–655
13. Samanta A, Mukhopadhyay M (1999) Finite element large deflection static analysis of shallow and deep stiffened shells. Finite Elem Anal Des 33:187–208
14. MacNeal RH (1998) Perspective on finite elements for shell analysis. Finite Elem Anal Des 30:175–186
15. Fahlström K, Andersson O, Todal U, Melander A (2005) “Minimization of distortions during laser welding of ultra-high strength steel. J Laser Appl 27:S29011
16. Tchoumi T, Peyraut F, Bolot R (2016) Influence of the welding speed on the distortion of thin stainless steel plates – numerical and experimental investigations in the framework of the food industry machines. J Mater Process Technol 229:216–229
17. Chen Z, Chen Z, Shenoi RA (2015) Influence of welding sequence on welding deformation and residual stress of a stiffened plate structure. Ocean Eng 106:271–280
18. Schenk T, Richardson IM, Kraska M, Ohnimus S (2009) Influence of clamping on distortion of welded S355 T-joints. Sci Technol Weld Joining 14(4):369–375
19. Schenk T, Richardson IM, Kraska M, Ohnimus S (2009) A study on the influence of clamping on welding distortion. Comput Mater Sci 45(4):999–1005
20. Ma N, Huang H, Murakawa H (2015) Effect of jig constraint position and pitch on welding deformation. J Mater Process Technol 221:154–162
21. Zhang C, Li S, Sun J, Wang Y, Deng D (2019) “Controlling angular distortion in high strength low alloy steel thick-plate T-joints. J Mater Process Technol 267:257–267
22. Lou M, Li Y, Cai W, Wang H, Carlson BE, Huang J, Poss MG (2020) Simulation of laser brazing of sheet panels and parametric studies of thermally-induced distortion reduction. Sme J Manuf Process 60:1–10
23. Thater R, Wiethop P, Rethmeier M (2015) Welding simulation in car body construction: virtual welding sequence planning for remote laser applications. Laser Tech J 12(2):33–37
24. Perret W, Schwenk C, Ethmeier MR, Raphael TR, Alber U (2011) Case study for welding simulation in the automotive industry. Weld World 55:89–98
25. Nateghi E, Volukola AG (2016) Experimental and numerical investigation into effect of weld configuration geometry on distribution of residual stress and temperature in the welded parts of stainless steel. Int J Adv Manuf Technol 87:2391–2404
26. Islam M, Bujik A, Rais-Rohani M, Motoyama K (2014) Simulation-based numerical optimization of arc welding process for reduced distortion in welded structures. Finite Elem Anal Des 84:54–64
27. Alro Steel “A1011 HSLA Steel Sheet”. www.alro.com/divsteel/metals_gridpt.aspx?gp=0057. Accessed 1 Sept 2021
28. Elsener B, Neubauer I, Khazan P, Gatzen M (2018) Simufact welding theoretical background manual. Simufact Engineering GmbH
29. Goldak J, Chakravarti A, Bibby M (1984) A new finite element model for welding heat sources. Metall Trans B 15(2):299–305